Measurements of the Trigger Rate of Drift Velocity Chambers

(Messungen der Trigger Rate von Driftkammern)

von

Jenny Tempeler

Bachelorarbeit in Physik

vorgelegt der

Fakultät für Mathematik, Informatik und Naturwissenschaften der RWTH Aachen

im August 2010

angefertigt im

III. Physikalischen Institut A

bei

Prof. Dr. Thomas Hebbeker

Ich versichere, dass ich die Arbeit selbstständig verfasst und keine anderen als die angegebenen Quellen und Hilfsmittel benutzt sowie Zitate kenntlich gemacht habe.

Aachen, den 1. August 2010 (Jenny Tempeler)

Contents

1 Introduction

Today's particle physics is interested in exploring the origin and the components of matter and its basic interactions. There are plenty of physical theories that intend to describe these phenomena, e.g. the Standard Model (SM), the Higgs mechanism or the Minimal Supersymmetric Standard Model (MSSM). However their correctness has to be proven with the help of experiments. So far the SM is the only theory that has been verified (more about the SM can be read in section 1.1 on page 4). There are two types of experiments with which physicists are able to investigate these theories: Either high energetic particles from the outer space are observed (AUGER[1]) or accelerated particles are brought to collision. The latter option is performed at CERN[2] situated in Geneva, Switzerland. There the greatest proton-proton accelerator, the LHC[3], is installed below the ground (fig. 1).

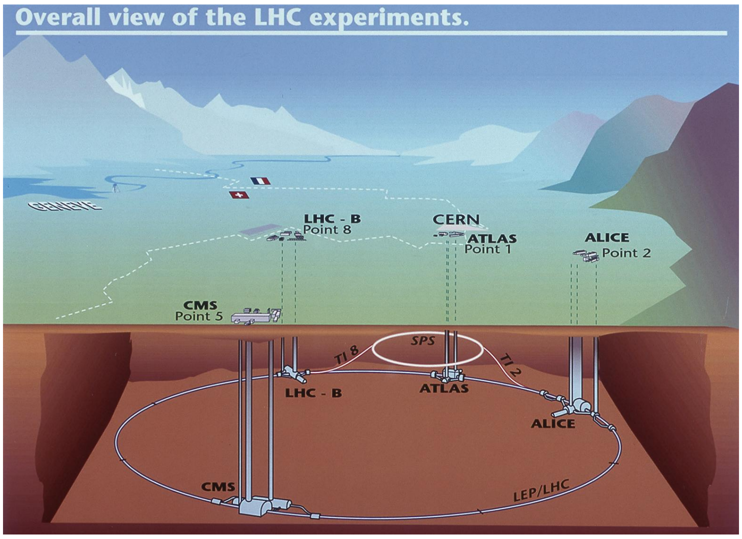

Figure 1: Overall view of the LHC and its experiments.[13]

The LHC is designed to collide protons (or heavy ions) which have a maximal kinetic energy of 7 TeV. Thar means they travel with 99.999 999 1 % of the speed of light. There are four interaction points at which the particles collide and the four major experiments are installed: ALICE,[4] ATLAS[5], CMS[6] and LHCb[7]. There, the newly created particles from the collisions are observed in large detectors. The ALICE experiment is specialized in examining quark-gluon plasma that is created during collisions of heavy ions. LHCb examines the occurrence of CP-violation during the production of b-mesons, i.e. the imbalance between matter and antimatter is analysed. ATLAS and CMS are multi-purpose detectors that search for new particles, especially the higgs boson. They are designed to crosscheck the results of each other. However, both experiments have a different physical approach to obtain results.

---

[1] Pierre-Auger-Observatorium
[2] European Organization for Nuclear Research
[3] Large Hadron Collider
[4] A Large Ion Collider Experiment
[5] A Toroidal LHC ApparatuS
[6] Compact Muon Solenoid
[7] Large Hadron Collider beauty e

The CMS detector is constructed like an onionskin. It has seven major layers of different detector types and components to obtain information, like the momentum and energy, about the newly created particles (see fig. 2): the silicon pixel tracker, the silicon strip tracker, the electromagnetic calorimeter (ECAL), the hadronic calorimeter (HCAL), the superconducting solenoidal coil, the iron yoke and the muon detectors. Detailed descriptions are given after the figure.

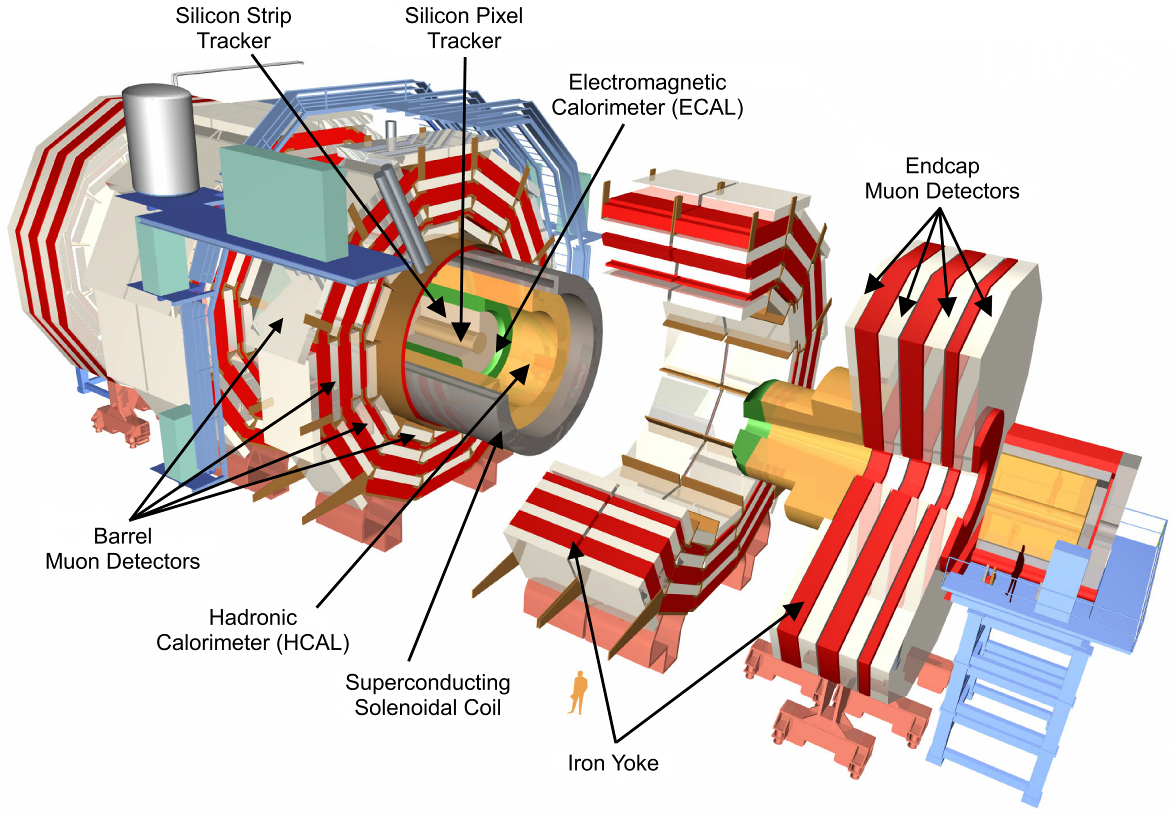

Figure 2: This figure gives an insight into the CMS detector and shows the location of the different components that are listed above. The detector has a diameter of 15 m and a weight of 15 t [14].

Silicon Pixel Tracker [15]

The silicon pixel tracker consists of three cylindrical layers wrapped around the beam pipe and of two disk-shaped layers that are installed perpendicularly to the beam pipe in the endcaps. The size of each pixels is 100 µm × 150 µm. Due to the set-up of in total 65 million pixels a radial resolution of 10 µm and in direction of the beam pipe of 20 µm is obtained. This part of the detector is able to track the paths of particles emerging from the collision with extreme accuracy.

Silicon Strip Tracker [17]

The silicon strip tracker is located behind the silicon pixel tracker. It consists of ten cylindrical layers in the centre and nine disk-shaped layers in the endcaps. The tracker and its electronics are cooled down to

$-20\,^\circ\mathrm{C}$ in order to prevent damage that is caused by radiation of particles. This detector is able to track high energetic particles for example leptons.

ECAL [17]

An electromagnetic calorimeter determines the energy of particles that interact electromagnetically with matter, for example photons and electrons. The incoming particle is completely absorbed by the detector material which in this case consists of 80 000 $PbWO_4$ crystals. During the process of absorption the lead tungstate crystals scintillate, i.e. the energy of the particles is converted to photons. This amount of light is detected by photodiodes and the energy of the particle can be reconstructed.

HCAL [17]

This kind of calorimeter determines the energy of hadronic particles like neutrons, kaons and pions. Also neutrinos can be detected indirectly due to missing energy and momentum. The HCAL is made of alternating layers of absorber (brass) and fluorescent scintillator materials. The deposited energy in each layer sums up to the energy of the particle.

Superconducting Solenoidal Coil [17]

A very strong magnet is needed to achieve a precise momentum resolution of high energetic particles in the muon system of the detector, because particles with high momentum bend less in the magnetic field ($F_L = F_Z \Leftrightarrow q \cdot v \cdot B = \frac{m \cdot v^2}{r}$). This solenoidal magnet, which is made of a titanium-niobium alloy, is built around the preceding detectors. It has a cylindrical shape with a diameter of 6 m and a length of 13 m. Furthermore the magnet is cooled down to $-270\,^\circ\mathrm{C}$ which leads to a magnetic field strength of 4 T.

Iron Yoke [17]

There are three cylindrical iron yokes installed in between the muon chambers that also bend incoming, high energetic particles due to magnetic induction.

Barrel Muon Detectors [16, 17]

The barrel muon detectors are located furthest apart from the interaction point. They are only reached by muons, neutrons and neutrinos. All other particles are absorbed by other detectors or have decayed beforehand. Neutrinos fly through the detector without leaving a track, because they hardly interact with matter. The tracks of muons are recorded with the help of 250 drift tubes (DT), 540 cathode strip chambers (CSC) and 610 resistive plate chambers (RPC). These detectors are arranged in cylinders around the beam line and in disks that cover the endcaps to obtain a three dimensional track of the particle.

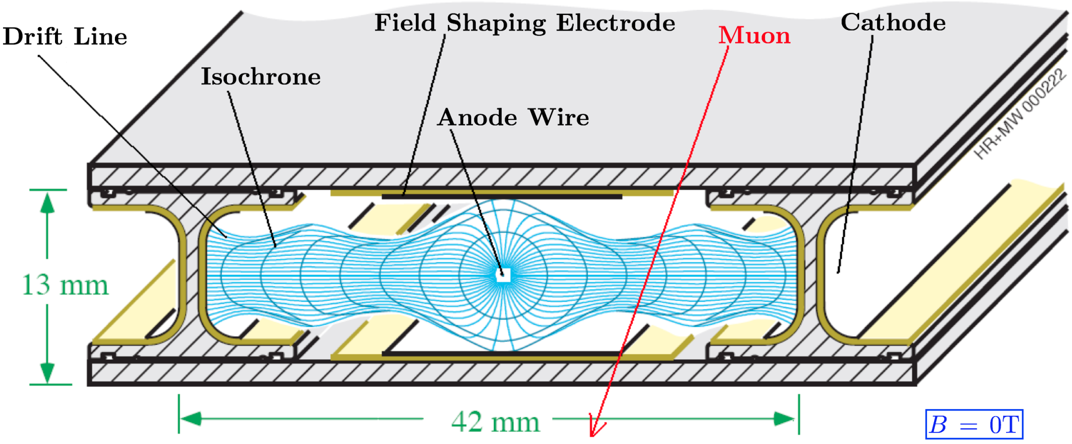

Figure 3: This is a cross-section of a drift tube[12, 8].

The drift tubes (fig. 3), which are a part of the muon system, have a length of $l = 42\,\text{mm}$ and a height of $h = 13\,\text{mm}$. The cathode is installed at the inside of the chamber wall and its voltage is set to 1200 V. The anode wire has a width of 50 µm and is situated in the centre of the chamber. Its voltage is set to 3600 V. A homogenous electric field is realised with the help of field shaping electrodes. The drift tube is filled with a gas mixture of argon (85 %) and carbon dioxide (15 %). A passing particle ionizes the gas molecules. The generated electron drifts towards the anode with an average drift velocity of $v_d = 55\,\mu\text{m}\,\text{ns}^{-1}$. The drift tube measures the drift time of the particle. Then the track of the passing particle can be determined in coherence with the drift velocity v_d. In the detector a positional resolution of 200 µm is obtained.

However the drift velocity is not constant over time and therefore needs to be monitored. In order to do so drift velocity chambers (VDCs) were invented. For the CMS experiment a system of at least five VDCs is needed, because the muon system is made of five large muon wheels which are filled with gas separately.

The VDC system in Aachen consists of six v_d-chambers (one is used as a spare) that can be filled with gas from each muon wheel. They are able to measure the drift velocity simultaneously with an accuracy of 0.2 % [1] during a measurement interval of 5 minutes. The trigger units of these VDCs, which generate the start signal of the drift time measurement, are the object of this bachelor thesis.

1.1 The Standard Model of Particle Physics

Elementary Particles of Matter

On the basis of experiments that have analysed matter up to the order of 10^{-18} m physicists assume that the universe consists of two types of elementary particles: leptons (tab. 1) and quarks (tab. 2). The particles' interactions, namely the weak, the strong, the electromagnetic and the gravitational one, are transmitted by the exchange of virtual particles: gauge bosons.

Particle / Antiparticle	Symbol	Family	Charge in e	Mass in MeV	Lifetime in s
Electron / Positron	$\mathrm{e}^- / \mathrm{e}^+$	I	-1 / +1	0.511	∞
Electron (Anti-)Neutrino	$\nu_\mathrm{e} / \bar{\nu}_\mathrm{e}$	I	0	$<2 \times 10^{-6}$	∞
(Anti-)Muon	μ^- / μ^+	II	-1 / +1	105.7	2.179×10^{-6}
Muon (Anti-)Neutrino	$\nu_\mu / \bar{\nu}_\mu$	II	0	< 0.19	∞
(Anti-)Tau	τ^- / τ^+	III	-1 / +1	1776	290.6×10^{-15}
Tau (Anti-)Neutrino	$\nu_\tau / \bar{\nu}_\tau$	III	0	< 18.2	?

Table 1: Table of leptons and their properties [10]

Leptons and quarks are particles with spin $\frac{1}{2}$ and are called fermions. There are six particles and antiparticles for each type that can be divided up into three families or flavours. The particles from the first family have the same physical properties than the ones from the second and third, e.g. the charge. They only differ in mass and lifetime.

Leptons can be found isolated, for example the electron e^- has the smallest charge that is observed among free particles: $1\ \mathrm{e} = 1.602 \times 10^{-19}\,\mathrm{C}$. Neutrinos are electrically neutral and have a very small, not yet determined mass. They hardly interact with other particles or matter.

Particle/Antiparticle	Symbol	Family	Charge in e	Mass in MeV	Color
(Anti-) Up	$\mathrm{u} / \bar{\mathrm{u}}$	I	$+\frac{2}{3}$	1.5 to 3.3	$r / g / b$
(Anti-) Down	$\mathrm{d} / \bar{\mathrm{d}}$	I	$-\frac{1}{3}$	3.5 to 6.0	$r / g / b$
(Anti-) Charm	$\mathrm{c} / \bar{\mathrm{c}}$	II	$+\frac{2}{3}$	1270	$r / g / b$
(Anti-) Strange	$\mathrm{s} / \bar{\mathrm{s}}$	II	$-\frac{1}{3}$	105	$r / g / b$
(Anti-) Top	$\mathrm{t} / \bar{\mathrm{t}}$	III	$+\frac{2}{3}$	171 300	$r / g / b$
(Anti-) Bottom	$\mathrm{b} / \bar{\mathrm{b}}$	III	$-\frac{1}{3}$	4200	$r / g / b$

Table 2: Table of quarks and their properties [10]

Quarks have an additional property: the colour charge. Each quark can either be red (r), green (g) or blue (b). Furthermore they can only exist in compound states, called hadrons that need to be neutral in colour towards the outside. This phenomenon is called colour confinement: The group of hadrons can be split into baryons, with three quarks of three different colours, and mesons, with two quarks of one colour and a matching anticolour. Their charge is $\frac{2}{3}$ e for the u-type and $-\frac{1}{3}$ e for the d-type quarks.

Matter itself is only made of leptons and quarks from the first family, because their lifetimes are infinite. For example two up and one down quark form a proton with charge $+1\ \mathrm{e} = \frac{2}{3}\ \mathrm{e} + \frac{2}{3}\ \mathrm{e} - \frac{1}{3}\ \mathrm{e}$.

Fundamental Interactions and Their Exchange Particles

Three of the four interactions that affect particles and matter are described by gauge theories in the standard model: QED[8] describes the electromagnetic interaction, QCD[9] describes the strong interaction and QFD[10] describes the unification of the electromagnetic and weak interaction [6]. Gravity is not included [4]. In total, there are twelve exchange particles (tab. 3) with spin 1 and they are therefore called (gauge) bosons.

Interaction	Exchange Particle	Symbol	Mass in GeV	Range in m	Strength
electromagnetic	Photon	γ	0	∞	$\frac{1}{137}$
weak	W-Boson	W^+ / W^-	80.3	10^{-18}	10^{-6}
weak	Z-Boson	Z^0	91.2	10^{-18}	10^{-6}
strong	8 Gluons	g	0	10^{-15}	1
gravitational	Graviton	G	0	∞	10^{-40}

Table 3: Table of gauge bosons and their properties [10]

The photon transmits the electromagnetic interaction between charged particles. It is massless, travels with the speed of light and its range is infinite.

The W- and Z-bosons cause the weak interaction. Since they are heavy particles, their range is limited and their effective strength is weak (at low q^2). Both W-bosons are able to convert the charge of the particle with which they are interacting. In contrast, the Z-boson conserves the charge due to its neutrality. An example for a weak interaction is the β^--decay: $n \longrightarrow p + e^- + \bar{\nu}_e$.

The strong interaction is mediated by eight gluons, which carry a colour and an anticolour. It is the reason why quarks can change their colour by emitting a gluon. This force also explains why the nuclear constituents stick together.

A graviton has not been discovered yet, which is supposed to describe the gravitational attraction. Therefore the gravitation is not included in the standard model.

Addition to the Standard Model

Looking at the masses of the particles, it can be seen that they vary within eleven orders of magnitude. However, the standard model does not describe the origin of the “weight”. A possible solution is the Higgs mechanism: This theory introduces a higgs field which couples to all particles. Its strength of coupling is proportional to the masses of the particles. The search of this particle is an aim of today’s research.

---

[8] quantum electrodynamics

[9] quantum chromodynamics

[10] quantum flavordynamics

1.2 Error Determination

In the following analysis sections, mostly counting rates are being examined. The error determination is explained here in order not to be redundant afterwards. All events are counted over a fixed time interval, which leads to the assumption that their number obeys a Poisson distribution. However when the average number of events, λ, which is the variance σ^2 at the same time, becomes large ($\lambda \rightarrow \infty$), the Poisson distribution approximates to a Gaussian distribution. Then the error of the number of events is given by the square root of itself. So the number of events is given by $n \pm \Delta n = n \pm \sqrt{n}$. However, there is no interest in the amount of events, but in the counting rate in Hz. Therefore the rate has to be calculated and the error has to be propagated, too. Then the counting rate is given by $r \pm \Delta r = \frac{n}{t} \pm \frac{\Delta n}{t}$, where t is the preset time interval. The error bars at each measuring point are not drawn in the plot, because they do not have an impact on the analysis. For example, at the determination of the working point it is important to understand the behaviour of the rates and the error on the measuring point can be neglected, because the weight of the error can be reduced by obtaining more statistics, i.e. the time interval of the measurement point is lengthened.

2 VDC System Aachen

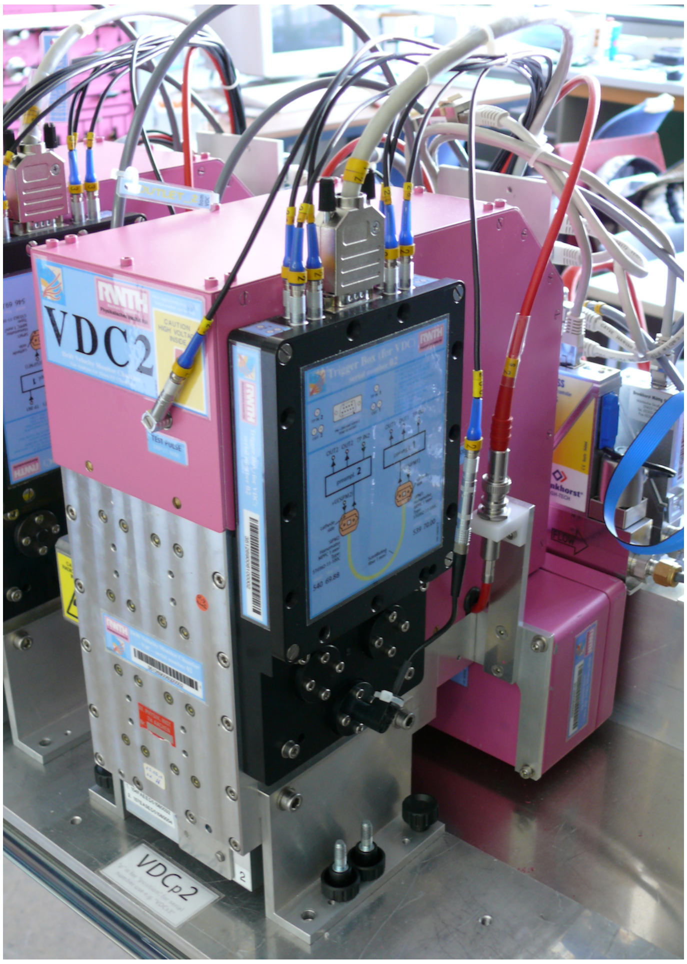

Figure 4: This photograph shows a VDC with a mounted trigger box as it is used in all measurements.

The drift velocity chambers (VDCs) are designed to measure the drift velocity v_d of electrons in gas continuously over time on conditions that are equal to those of the large muon chambers. Later, the gas that has to be analysed comes from the large muon barrels at the CMS detector. As there are five barrel wheels and each is separately filled with gas, there is a need for at least five VDCs. A sixth chamber is foreseen to be used as a spare and can crosscheck the measurements of another chamber. Also, with this number of v_d-chambers systematic and statistical errors can be assessed.

2.1 Experimental Set-Up and Functioning

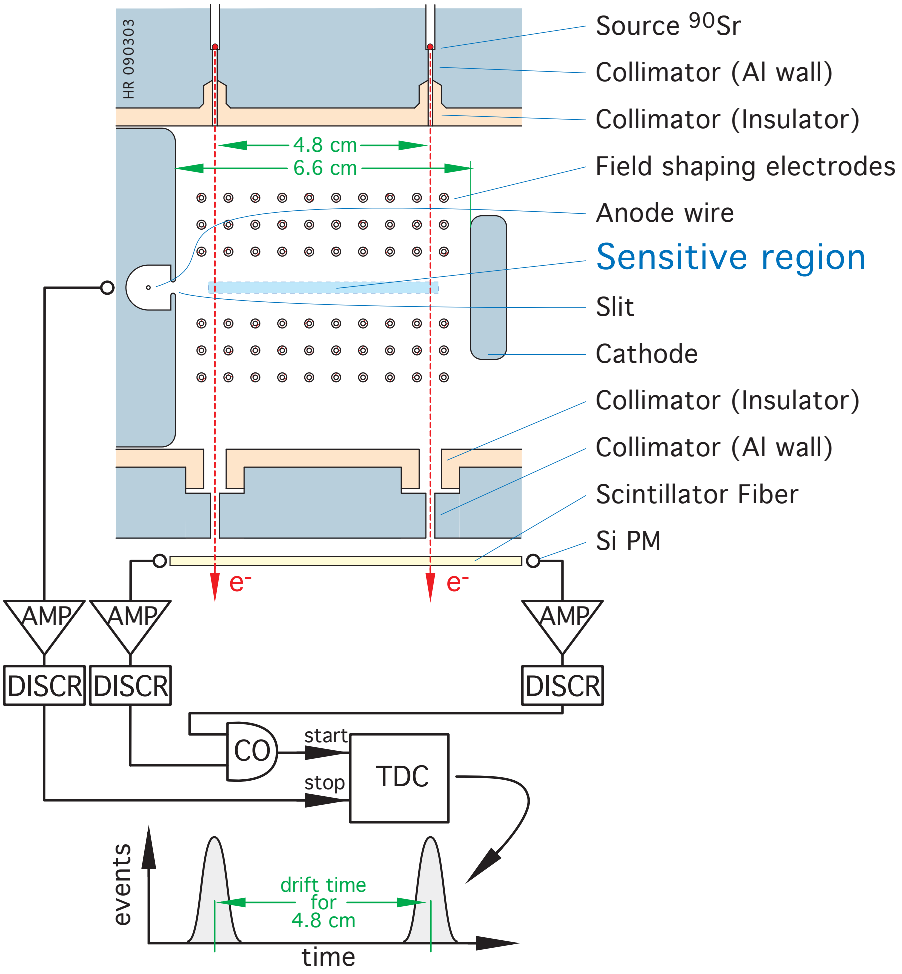

Figure 5: This true to scale drawing shows the set-up of the inside of the VDC [12].

All chambers have an aluminium casing which is wrapped around about 1 l of gas volume, see fig. 5. There are two inlets for the β^--decay electrons that come from two different, adjoining Sr^{90} sources. Both have an activity of 10 MBq. These electrons travel through the gas volume and ionize the molecules. They exit the chamber on the opposite side through two outlet slits and hit a scintillating fibre on the inside of the trigger box (section 3.1 on page 12). The generated light pulses are registered by two silicon photomultipliers (SiPMs). Inside the drift chamber, there are two sets of field shaping electrodes that create a so-called "sensitive region" in which the electrons from the ionization drift towards the anode in a highly homogenous electric field ($\frac{\delta E}{E} = 0.1\,\%$) [2]. The anode voltage is set between 1850 V and 2000 V[11]. The ions are captured by field shaping electrodes and the cathode. The cathode voltage is set to -14 kV, which causes a field strength of 200 V mm^{-1} which is identical to the field strength of the muon chambers.

---

[11] The exact values are determined by Jennifer Arps [1]

2.2 Determination of the Drift Velocity

Each drift velocity chamber yields three signals that are used to determine the drift velocity: Two signals from the SiPMs and one from the anode. A fourth signal is generated with a coincidence module that combines the signals from both SiPMs to the trigger. This process is described in detail in section 3.1 on page 12. The trigger represents the start of the drift time measurement and verifies that this signal is caused by an electron from the β^--decay and not by noise. The anode signal defines the end of the drift time so that a long and a short drift time (t_1 and t_2) is obtained (fig. 6). The concept of using two radioactive sources and therefore two drift times for the calculation of the drift velocity is due to A. Böhm et al. [3]. It is convenient, because all systematical errors concerning the electronical devices cancel out.

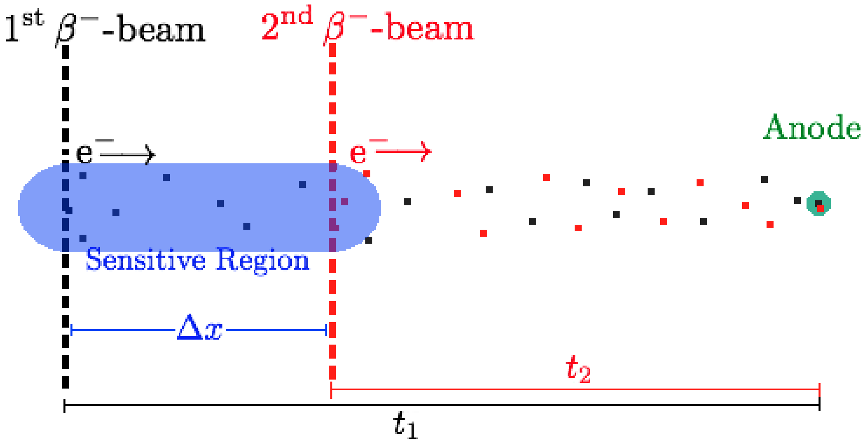

Figure 6: This outline explains the origin of the different drift times t_1 and t_2 and shows the geometrical relation to calculate the drift velocity v_d.

With these quantities the drift velocity v_d can be calculated within the homogenous electric field, i.e. the sensitive region, over a length of $\Delta x = 48\,\text{mm}$:

$$v_d = \frac{\Delta x}{t_1 - t_2} \tag{1}$$

The measured drift times are filled in a histogram in which two peaks can be observed. One peak for the short and one for the long drift time. At each peak the mean value and its error of a Gaussian distribution fit is used for the calculation of the drift time so that the statistical error is minimized. The following plot (fig. 7) shows the result of a drift time measurement:

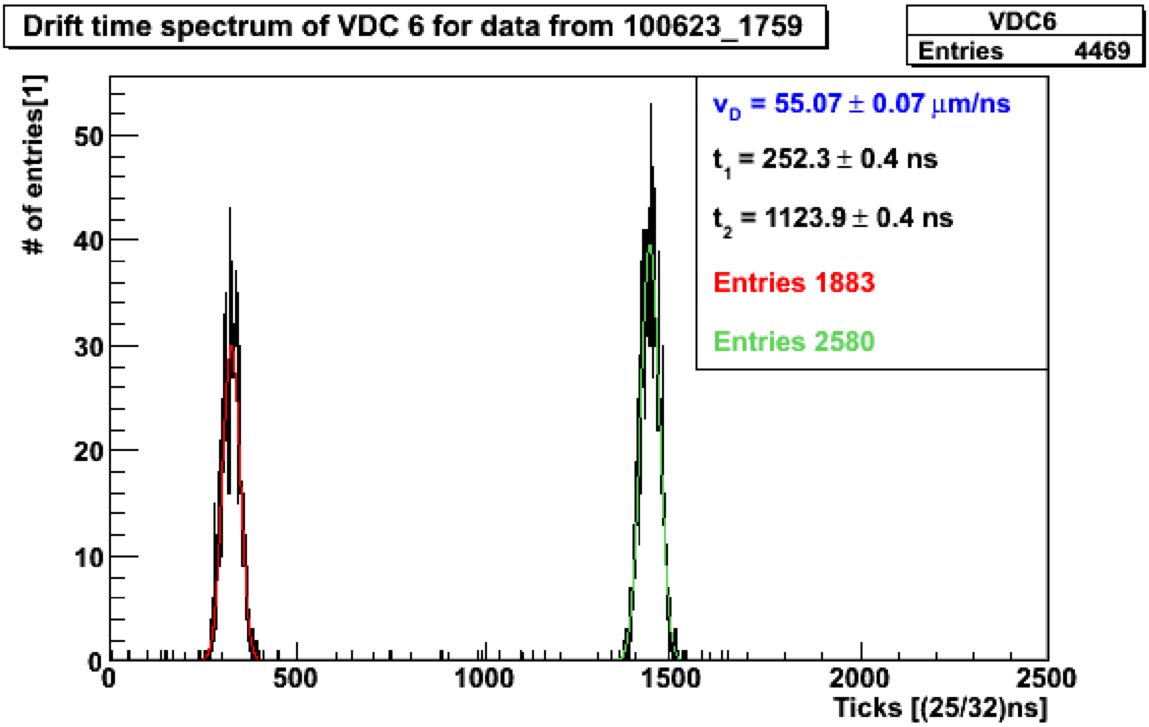

Figure 7: This is a typical drift time spectrum measured over a time period of 5 minutes, including two Gaussian distributions (red and green) that are fitted to the peaks [1]. Also both calculated drift times and the determined drift velocity are given.

More information about the determination of the drift velocity, the characteristics of drift time spectra and the VDC itself can be obtained from Jennifer Arps' bachelor thesis: "Measurements of the Drift Velocity in Drift Velocity Chambers (VDC)" [1].

3 Trigger System

The task of the trigger system is to start the drift time measurement. It should also separate effectively real signals of the chamber from noise background, because it is the aim to achieve a high trigger rate while excluding as much noise as possible. Regarding this, the working point of the SiPMs can be determined.

3.1 Experimental Set-Up and Functioning

The construction and the set-up of this trigger box are a result of Hans Reithler [12] and Jens Frangenheim's diploma thesis [9] and is shown in figure 8. The trigger box consists of two silicon photomultipliers[12] (SiPMs) which are connected via a u-shaped scintillating fibre[13]. There are two outlet slits through which the electrons from the drift chamber enter the trigger box. In addition, a LED[14] is installed on top of the fibre to test the efficiency and the timing of the trigger system.

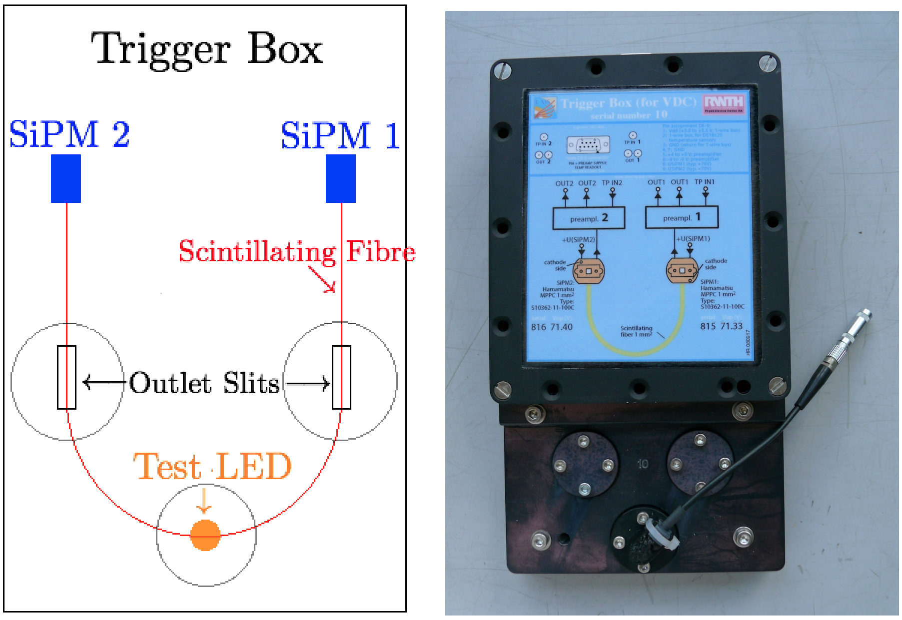

Figure 8: The outline (figure on the left) shows the set-up of the trigger box and its important parts, i.e. the outlet slits, that cannot be seen from the outside (photograph on the right).

A signal at both SiPMs is generated due to only one β^--decay electron because they are connected via a scintillating fibre with a length of $l = 30\,\mathrm{cm}$ (fig. 8): The electron either exits the drift chamber at the right or left outlet slit and generates photons inside the fibre. These photons have to travel a short and a long distance to either SiPM. However the maximal time t_{max} that a photon would need to travel from one end of the fibre to the other can be calculated:

$$c' = \frac{c}{n} \tag{2}$$

---

[12] Type: Hamamatsu MPPC $1\,\mathrm{mm}^2$ S10362-11-100C

[13] Type: BCF-12MC

[14] Light Emitting Diode

$$t_{max} = \frac{l}{c'} \tag{3}$$

c is the speed of light, $n = 1.5$ is the refraction index of the fibre and c' the propagation velocity of the photon inside the scintillating fibre. This leads to $t_{max} = 1.5\,\text{ns}$.

Subsequently the generated photons are detected by two MPPCs[15] (SiPM1 & 2) that have an effective area of 1 mm × 1 mm which is sensitive for the range of wavelengths from 320 nm to 900 nm. The MPPC is a kind of SiPM which is especially designed to count photons and consists of multiple APD[16] pixels operating in Geiger mode. The signal output is equal to the sum of all incoming photons [5].

Afterwards two preamplifiers increase each signal coming from the SiPMs and two discriminators convert them to NIM-pulses with a length of $l_{NIM} = 25\,\text{ns}$, if the amplitude of the signal is equal or greater than the preset discriminator threshold.

Because the maximal time difference t_{max} is small compared to the generated pulse at the discriminator (about 15 times smaller), both signals from the SiPMs are combined to the trigger rate with the help of a coincidence module. This verifies that the start signal for the drift time measurement, i.e. the trigger, is due to a β^--decay electron and not due to random noise pulses. The following figure visualizes the signal path which is explained above.

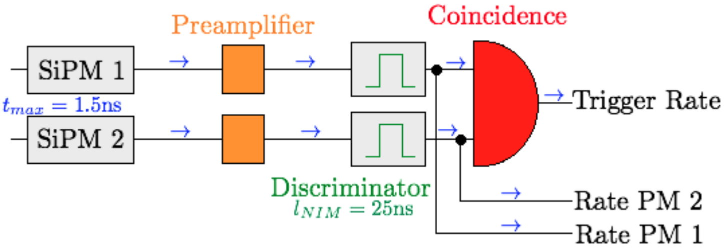

Figure 9: This outline shows the signal path of the trigger system and the origin of the counting rates.

All signals are counted and recorded in different rates called PM 1, PM 2 and trigger (fig. 9), because they are needed to analyse the trigger system.

3.2 SiPMs: Characteristics and Expected Rate Values

With the help of the geometry of the chamber and the characteristics of the radioactive Sr^{90} source, predictions can be made about the expected, maximal counting rate at each SiPM. Also, a statistical estimation of the random coincidence rate, which influences the trigger rate, can be calculated. In addition, some general information about the characteristics of SiPMs regarding temperature and noise are given.

---

[15] multi-pixel photon counter

[16] Avalanche Photo Diode

3.2.1 Counting Rate

The Sr^{90} source is a β^--emitting nuclide that decays into Y^{90} with a maximum decay energy of E_{max} = 0.55 MeV. The decay product Y^{90} is also a β^--emitter, but with a higher maximum decay energy of E_{max} = 2.28 MeV. However, the mean energy of the decay electrons is only one third of E_{max} [11]. Because of that only a fraction (about one third), with energy greater than 1.2 MeV [2], reaches the scintillating fibre.

$$\mathrm{Sr}^{90} \longrightarrow 0.55\mathrm{MeV} \longrightarrow \mathrm{Y}^{90} \qquad \text{half life: } 28.5\mathrm{a}$$

$$\mathrm{Y}^{90} \longrightarrow 2.28\mathrm{MeV} \longrightarrow \mathrm{Zr}^{90} \qquad \text{half life: } 64.1\mathrm{h}$$

As seen in fig. 10, the Sr^{90} source is located behind a cylindrical collimator with a diameter of $d_1 = 1$ mm and a length of $b_1 = 17$ mm which leads a fraction of the β^--rays into the inside of the chamber which has a total length of $l = 75$ mm. The collimation of the electrons from the β^--source is constructed so that none are captured by field shaping electrodes before they are arriving at the sensitive region. Then the electrons have to exit the chamber through a second, rectangular shaped outlet slit with a height of $d_2 = 10$ mm and a width of $b_2 = 2$ mm. However, the scintillating fibre which is installed right behind the outlet slit only has a width of $d_3 = 1$ mm and therefore reduces the area in which the arriving electrons can generate photons that are detected by the SiPMs. The following figure shows the geometrical relations inside the trigger box.

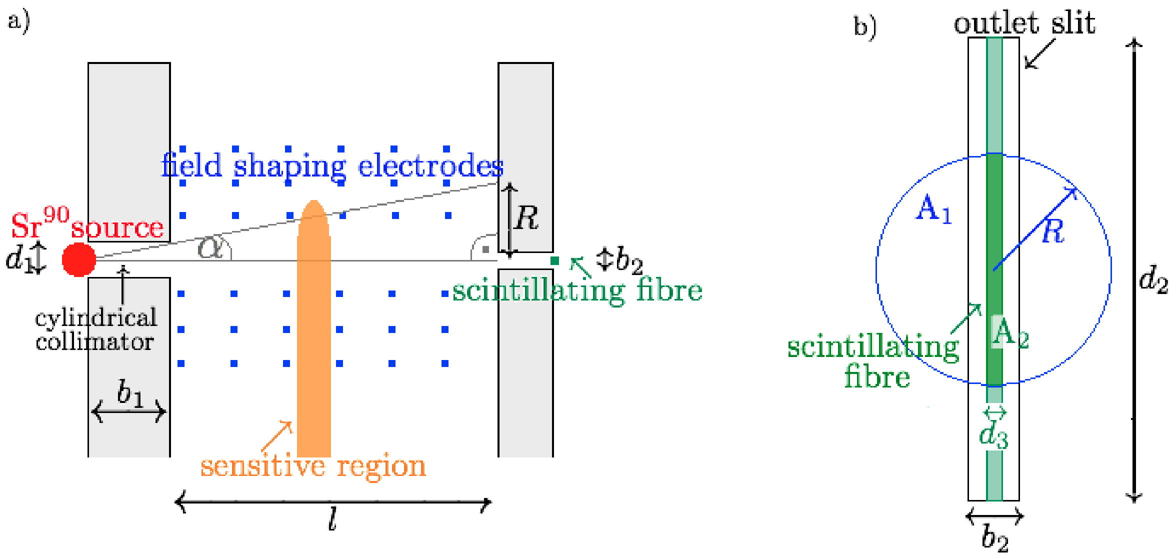

Figure 10: a) shows the top view from one half of the inside of the VDC. b) presents a close-up of the chamber wall in which the outlet slit is positioned. Both figures show the geometrical relations that are needed for the calculation of the expected counting rate at each SiPM.

Requiring that the radioactive source with an activity $A = 10$ MBq can be regarded as a point source, the ratio of the aperture angle Ω to the solid angle $\Omega_{total} = 4\pi$ can be calculated:

$$\begin{aligned}
\alpha &= \arctan\left(\frac{d_1}{2b_1}\right) \approx \frac{d_1}{2b_1} \approx 1.7^\circ && (4)\\
\Omega &= \int_0^{2\alpha} \sin\vartheta \, d\vartheta \int_0^{2\pi} d\varphi \approx 0.0027 && (5)\\
\frac{\Omega}{\Omega_{total}} &= 0.0002 && (6)\\
A \cdot \frac{\Omega}{\Omega_{total}} &\approx 2.16 \text{ kHz} && (7)
\end{aligned}$$

The amount of electrons from the β^--decay (eq. 7) that have found their way into the chamber is given by $2 \cdot 2.16\text{kHz} = 4.32\text{kHz}$, because there are two Sr^{90} sources installed at each VDC that emit β^--decay electrons. Neglecting energy loss due to ionization and collisions with other particles which cause a change of direction of the flight path, the area A_1 represents the area that can be reached by particles from the radioactive source. Only electrons in area A_2 can also reach the scintillating fibre. A_2 can be approximated to a rectangle, because the width of the fibre d_3 is small compared to the height of the rectangle which is equal to the diameter $2R$. Again, this fraction reduces the number of particles by the ratio of A_2 to A_1.

$$\begin{aligned}
A_1 &= \pi R^2 && (8)\\
R &= \frac{d_1 \cdot (b_1 + l)}{2b_1} \approx 2.7 \text{ mm} && (9)\\
A_2 &\approx 2 \cdot R \cdot d_3 && (10)\\
\frac{A_2}{A_1} &= \frac{4 \cdot d_3 \cdot b_1}{\pi \cdot d_1 \cdot (b_1 + l)} \approx 0.24 && (11)\\
\Rightarrow A \cdot \frac{\Omega}{\Omega_{total}} \cdot \frac{A_2}{A_1} \cdot \frac{1}{3} &\approx 169 \text{ Hz} && (12)
\end{aligned}$$

Furthermore, assuming that only about one third of the β^--rays have enough energy to cause a signal (see eq. 12) leads to a maximal counting rate at each SiPM of 169 Hz.

The ratio of electrons inside the chamber, which ionize gas molecules, to the amount of electrons that cause a signal at the SiPMs is about $\frac{2 \cdot 2160}{2 \cdot 169} \approx 12.8$. The amount of electrons inside the chamber is about 13 times greater than the amount that exit the chamber. This difference can be explained with the geometry of the chamber: most electrons cannot escape through the small outlet slit.

3.2.2 Accidental Coincidence

A random coincidence describes the quasi simultaneity of two pulses (mainly noise pulses) that generate a trigger signal that is not caused by β^--decay electrons and is therefore an incorrect start signal for the drift time measurement.

Random or accidental coincidences occur due to background noise, a finite pulse width set at the discriminator output and the propagation time of light within the scintillating fibre. The actual trigger rate at the working point should have as little noise as possible. With a statistical calculation of the random coincidence rate a range in which the noise is dominant can be excluded.

For the calculation, the adjusted pulse length of both discriminators l_{PM1} and l_{PM2} is needed and the maximal time difference between two pulses Δt is as well given by the coincidence unit. Also, both independent counting rates n_1 and n_2 from the SiPMs have to be determined. Then the random coincidence rate n_{12} is given by [9]:

$$n_{1,2} \quad = \quad (l_{PM1} + l_{PM2} - \Delta t) \cdot n_1 \cdot n_2 \tag{13}$$

This quantity is calculated and drawn in all plots for measurements in which SiPMs are involved. For example, when two pulses have a length of 25 ns and they have a maximal time difference of $\Delta t = 0.1\,\mathrm{ns} \approx 0$, a random coincidence of about 5 MHz is obtained when both independent counting rates are given as $n_1 = n_2 =$ 10 MHz.

3.2.3 Temperature and Noise

The SiPMs are very sensitive to temperature, for example at 21 °C (room temperature) the noise rate is about 3 MHz to 10 MHz [12]. This rate had to be reduced, because the expected counting rate from β^--events at each SiPM (sec. 3.2.1 on page 14) is up to five orders of magnitude smaller than the noise (sec. 3.2.2). This can be achieved by operating the SiPMs in a cooled environment of −20 °C. However, in this set-up the space is limited and a cooling system would be expensive, cumbersome and difficult to integrate in an environment at room temperature. So the problem is solved with the help of a coincidence module. Then the generated trigger rate $n_{trigger}$ is equal to the real number of electrons n_{signal} that reach the SiPMs plus the random coincidence n_{noise} that is due to noise.

$$n_{trigger} = n_{signal} + n_{noise} \tag{14}$$

In order to receive an overview of the size of the reduction that is due to the coincidence module, the ratios $\mathrm{R}_{red,\,i}$ of the trigger rate $n_{trigger}$ to the PM counting rates n_i (with i=$PM1$ or $PM2$) at the working point (tab. 16 on page 22) are calculated and listed below.

$$\mathrm{R}_{red,\,i} = \frac{n_{trigger}}{n_i} \tag{15}$$

The data that are analysed can also be seen in figure 13 on page 19.

VDC Position/Serial No.	3	4	5	6
$\mathrm{R}_{red,\,PM1}$	0.40	0.34	0.29	0.32
$\mathrm{R}_{red,\,PM2}$	0.01	0.20	0.33	0.40

Table 4: The calculated ratio of the trigger rate to the PM counting rates (according to equation 15) is listed in this table for four different VDCs.

To conclude, about 30 % of all incoming signals at the working point are real signals caused by β^--decay electrons. The remaining 70 % are noise signals that are filtered by the coincidence. There is one exception (VDCp3/PM 2) with a ratio more than ten times smaller. This indicates that the noise of this SiPM is greater compared to the other ones. This can be explained due to a false working point or high temperatures. The coincidence module proves useful as an effective solution to reduce noise and as being able to generate a clean trigger signal.

3.3 Determination of the Working Point

It is not possible to obtain a clean trigger rate with signals only coming from the Sr^{90} sources, because noise is always present. However, a convenient compromise can be found in which the trigger rate is high enough in order to provide a sufficient number of start signals for the drift time measurement and is not dominated by noise. It is the aim of this analysis section to determine these so-called working points for all SiPMs that fulfil the mentioned criteria. As a result, a table is presented in which the working points are listed in dependence on the discriminator threshold (PM threshold). The final PM threshold is determined with the help of the TDC data in Jennifer Arps' bachelor thesis[1]: It is observed which combination of PM and anode threshold is the most effective in view of the amount of entries of the drift times in the histogram for the determination of the drift velocity (sec. 2.2 on page 10).

3.3.1 Parameters

The parameters that have an impact on the working point are the supply voltage of the SiPMs and the thresholds at the discriminators. The temperature also affects the working point, but this influence is due to the surrounding environment and therefore it cannot be varied on purpose.

The manufacturer of the photomultipliers, Hamamatsu, states that the SiPMs can be operated at a voltage of 70±10 V. In addition, an operating voltage is given for each SiPM (tab. 6 on page 23) [5]. However, these values need to be verified whether it is suitable for the drift time measurements or not. Therefore, the range from 68.1 V to 71.5 V in steps of 0.1 V is analysed (this kind of measurement is called "run type PM"). The discriminators behind the SiPMs define which pulse height is needed to generate a signal that can be used for the counting rates. This threshold is varied in between the measurements.

3.3.2 Run Type PM

In all following figures both PM rates, the trigger rate and the accidental coincidence rate (sec. 3.2.2 on page 15) are shown. Also, the ratio of the accidental coincidence to the trigger rate is drawn in the plot. On the basis of this overall view it is possible to determine the working point. But first, a useful range for the working point has to be identified by understanding the different counting rates with regard to a logarithmic scale on the y-axis.

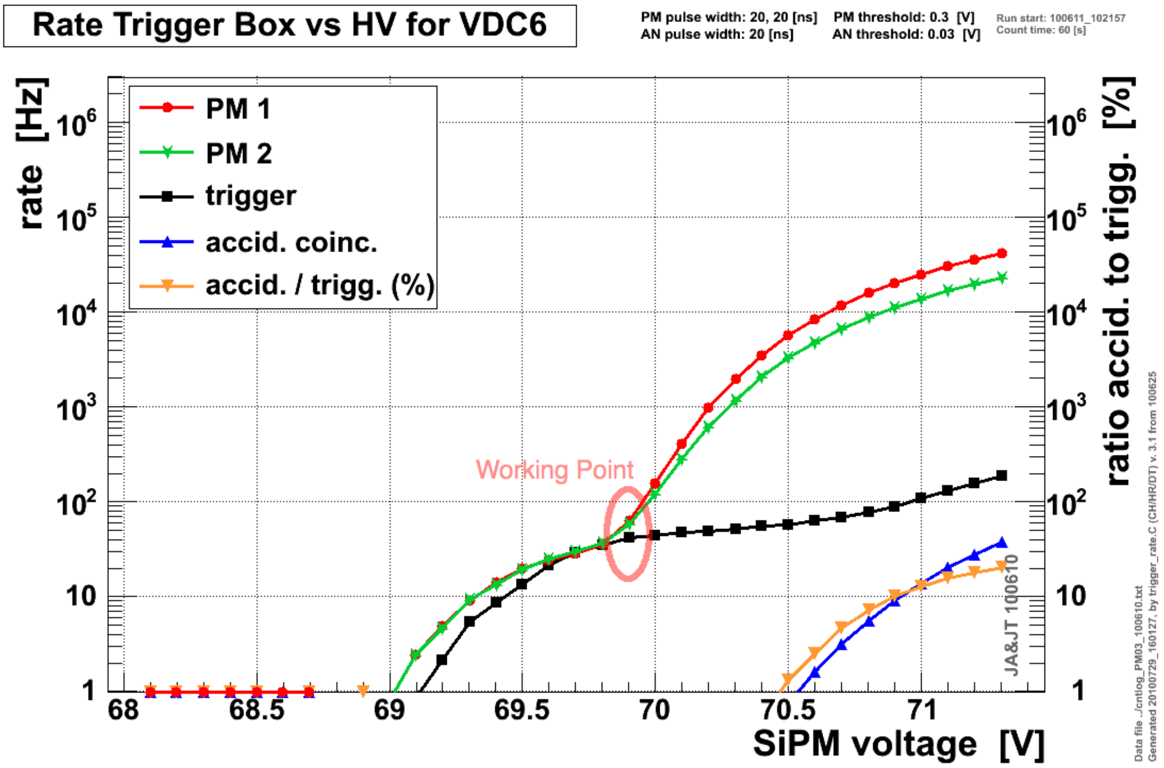

Figure 11: The PM Threshold is set to 0.3 V. The SiPM voltage at the working point is 69.9 V.

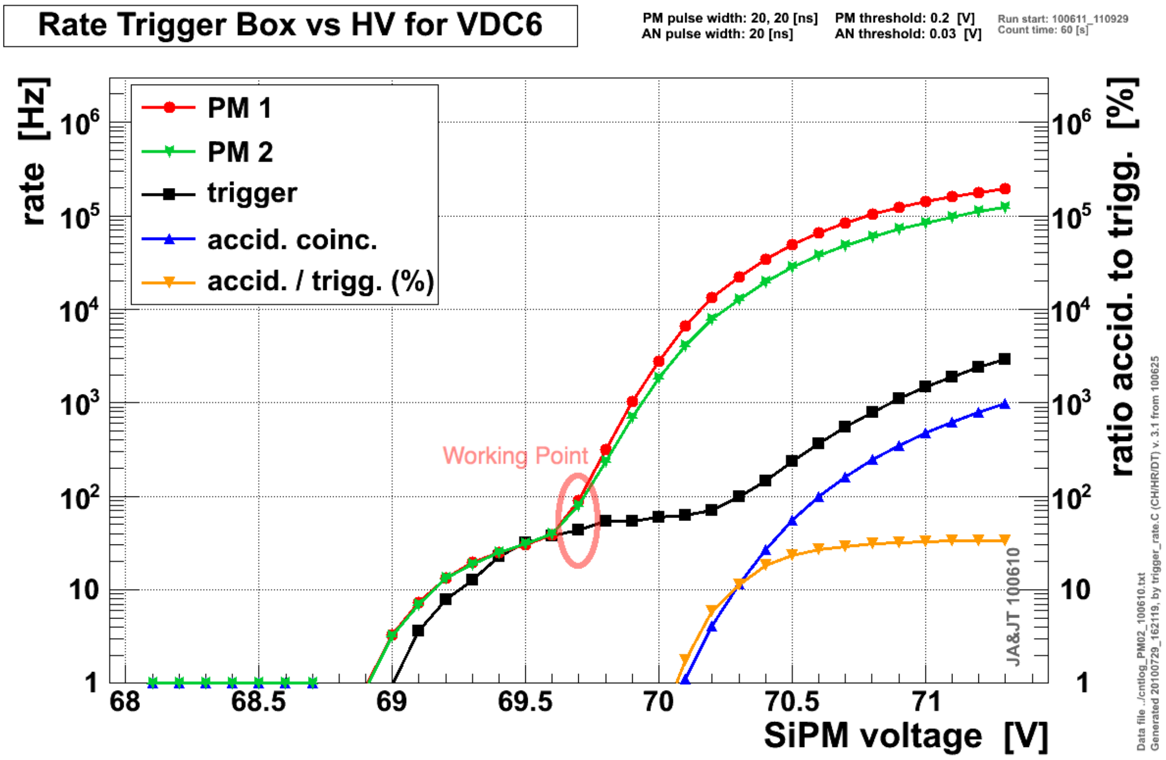

Figure 12: The PM Threshold is set to 0.2 V. The SiPM voltage at the working point is 69.7 V.

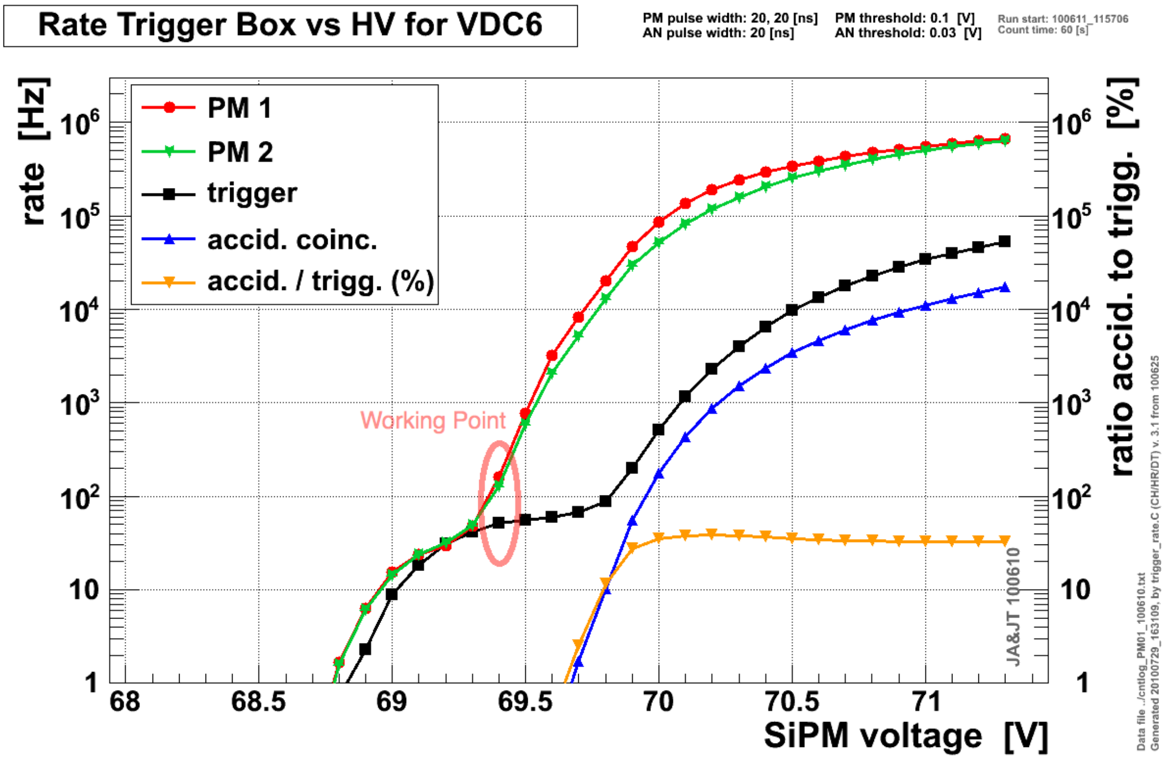

Figure 13: The PM Threshold is set to 0.1 V. The SiPM voltage at the working point is 69.4 V.

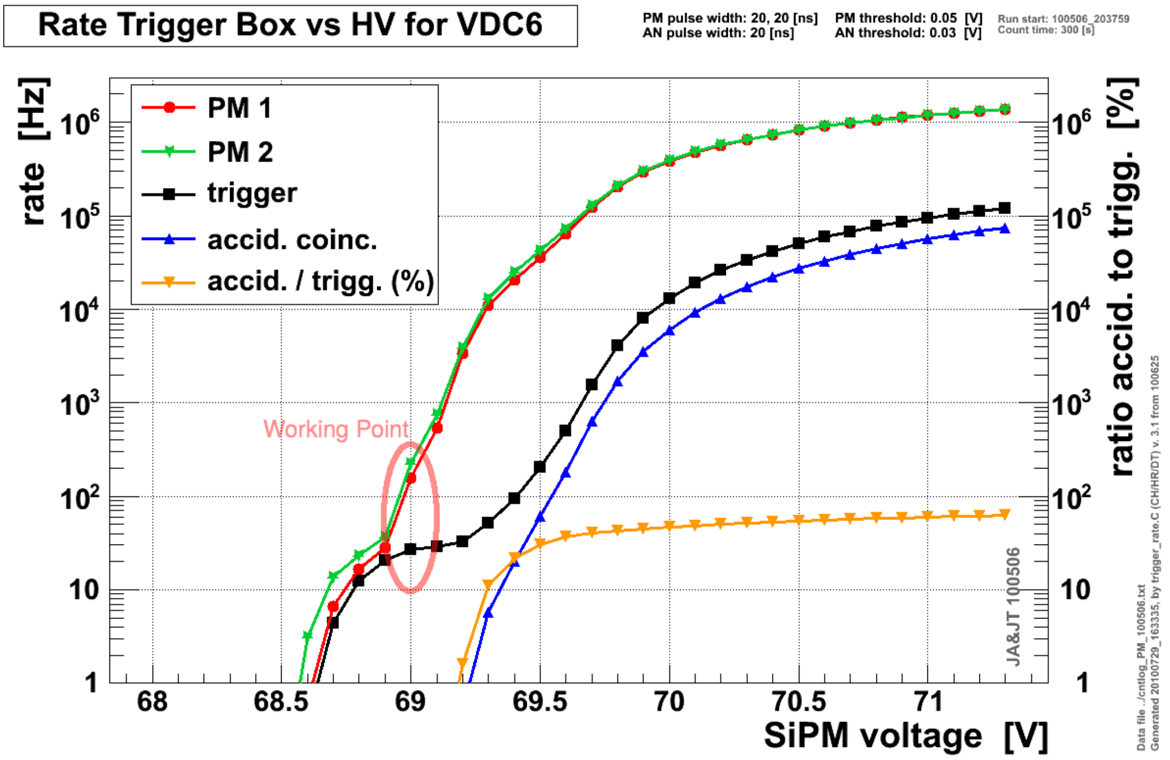

Figure 14: The PM Threshold is set to 0.05 V. The SiPM voltage at the working point is 69.0 V.

The progression of the counting rates versus the SiPM voltage is the same in all four plots (fig. 11 - 14) with different PM thresholds (0.05 V to 0.3 V): At the beginning both PM rates and the trigger rate are increasing simultaneously, because more and more pulses are seen until the trigger rate reaches a first plateau. This means that the counting rates increase exponentially along with the supply voltage. However, at the beginning of the trigger plateau the PM counting rates separate from the trigger rate and the ascent of the PM rates is steep and is dominated by noise from now on. As long as the trigger rate is forming a plateau, the coincidence module still distinguishes between real events from the source and noise. It is reasonable to choose the working point in the first plateau area, because the trigger rate is maximal with little or no noise. After the trigger plateau the trigger rate also increases immensely, because now the accidental coincidence rate becomes dominant due to the large amount of noise pulses at the SiPMs and again flattens out on a second plateau. This means that the noise rate increases linearly.

To summarize, the counting rates can be divided up into a part in which the signals from the β^--decay electrons are dominant and into another one in which the noise is dominant. The first part increases exponentially with the SiPM voltage and the second part linearly. Both parts overlap in the counting rates. Noise measurements (fig. 15) were done in which no Sr^{90} sources are installed inside the VDC and therefore only noise signals are measured. Due to the fact that the random coincidence rate describes the number of random, but coincidental noise pulses, the trigger rate should be the same as the accidental coincidence rate. As it can be seen in the plot, both rates differ slightly for high SiPM voltages ($\geq$70 V). This can be due to the large number of noise pulses that affect the trigger rate more than expected compared to the calculated random coincidence rate. To proof whether the VDC also generates noise or not, another noise measurement with only a trigger box, i.e. no VDC is installed, has been made. However, the rates in these two measurements are the same so that it can be assumed that the noise mainly comes from the trigger box.

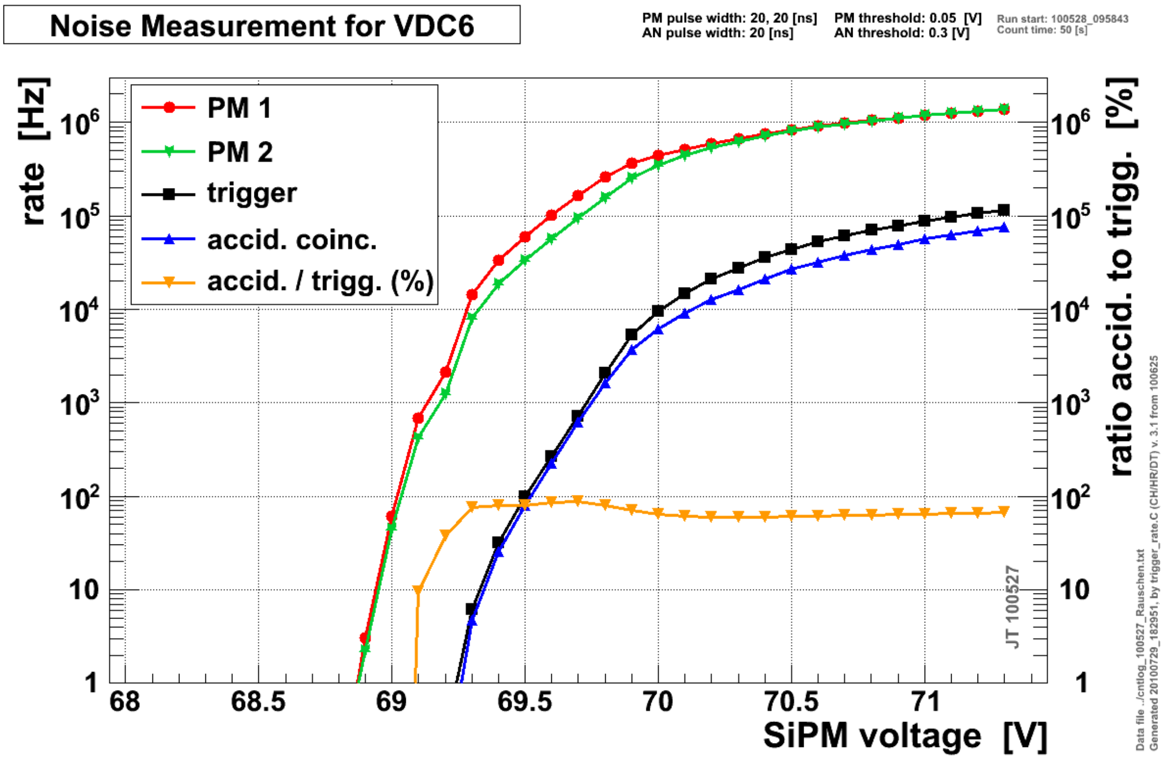

Figure 15: This is the plot of a noise measurement during which no Sr^{90} sources were installed inside the VDC

Comparing the four plots (fig. 11 to 14) with each other, it can be seen that the trigger plateau becomes shorter while the PM threshold becomes smaller. This behaviour can be explained: With a small PM threshold more pulses come out of the discriminator and reach the coincidence. It implies that more noise pulses do so as well and that therefore they dominate the trigger rate at lower SiPM voltages.

3.3.3 Analysis of Counting Rates

Referring to the description above, the working point is defined at the beginning of the first plateau, for example in figure 13 marked with a red circle at 69.4 V. There the SiPM rates start to separate from the trigger rate and a clean trigger rate can be obtained. Also, there is room for variation to higher and lower SiPM voltages in which the trigger rate is almost constant and the signal stays clean of noise. It is reasonable to choose the same working point for both SiPMs as long as the rates of PM 1 and PM 2 have a similar curvature. Also during the set-up, pairs of SiPMs with similar characteristics were selected for the installation in each trigger box. In the following table (tab. 5) all working points are listed for the different VDCs. In addition, the following plot (fig. 16) shows the working points of the different VDCs versus the PM threshold.

			PM Threshold in V			
VDC Pos.	VDC Serial No.	Trigger Box Serial No.	**0.05**	**0.1**	**0.2**	**0.3**
3	3	7	69.7	70.0	70.4	70.6
4	4	4	69.5	69.9	70.3	70.5
5	5	5	69.3	69.5	69.9	70.1
6	6	6	69.0	69.4	69.7	70.0

Table 5: List determined working points for all VDCs in dependence on the PM threshold at the discriminator.

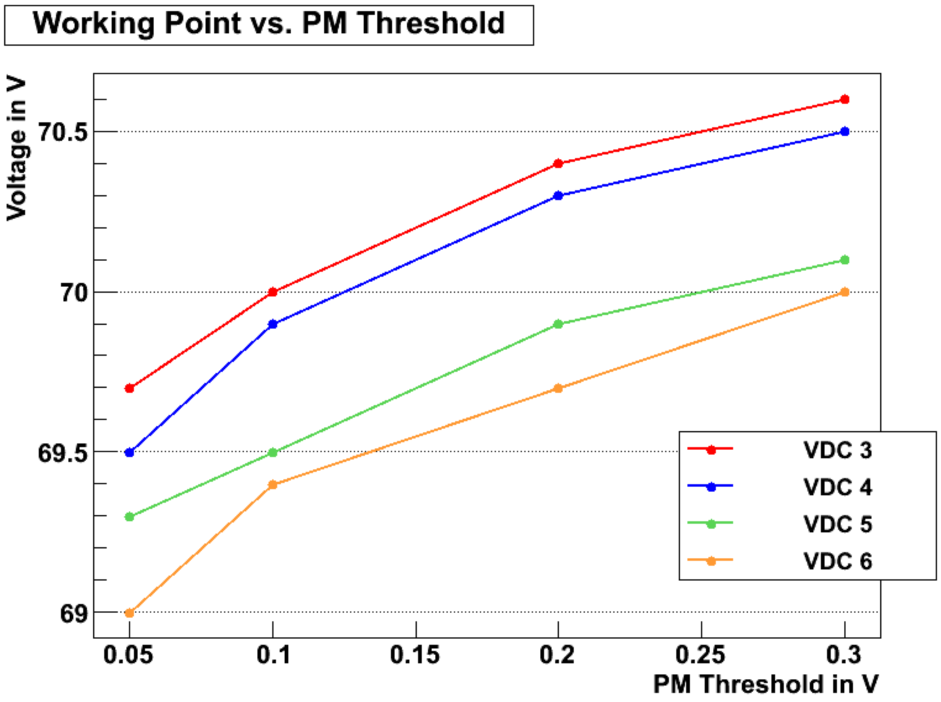

Figure 16: A linear dependence of the voltage of the working point to the PM threshold at the discriminator can be observed for all four chambers.

From the figure above, a linear relation between the PM threshold and the working point can be assumed. The deviations from the linear dependence are caused due to the fact that the measurements have been taken on different days and only data from one measurement have been analysed in order to find the working point for a trigger box.

The conclusion can be drawn that not only one working point for each SiPM, given by the manufacturer Hamamatsu (tab. 6 on the following page), is sufficient, because in this set-up the working point depends on the discriminator threshold. Also, the SiPM voltage cannot be adjusted with the same precision than given by Hamamatsu. The supply voltage varies up to $\pm 0.04\,\mathrm{V}$. Comparing the given working points to the experimentally determined ones, it can be observed that they only match for small PM thresholds (0.05V and 0.1V). Unfortunately, there is nothing to find about Hamamatsu's determination of the working point, so that a proper comparison of the working points is not possible.

Working Point in V for	PM Threshold in V	Trigger Box Serial No. 2	4	5	6	7	9
SiPM 1 (Hamamatsu)	?	70.00	69.96	69.41	69.43	69.87	71.24
SiPM 2 (Hamamatsu)	?	69.88	69.99	69.34	69.43	69.57	69.34
SiPM1&2 (Measured)	0.05	n/a	69.5	69.3	69.0	69.7	n/a
SiPM1&2 (Measured)	0.1	n/a	69.9	69.5	69.4	70.0	n/a
SiPM1&2 (Measured)	0.2	n/a	70.3	69.9	69.7	70.4	n/a
SiPM1&2 (Measured)	0.3	n/a	70.5	70.1	70.0	70.6	n/a

Table 6: All working points that given by Hamamatsu and the ones determined in the analysis are listed in this table.

The next four plots show the trigger rates in Hz at different working points. Four rectangular distributions can be observed which state that a stable and clean trigger rate has been found and it does not change at different PM thresholds.

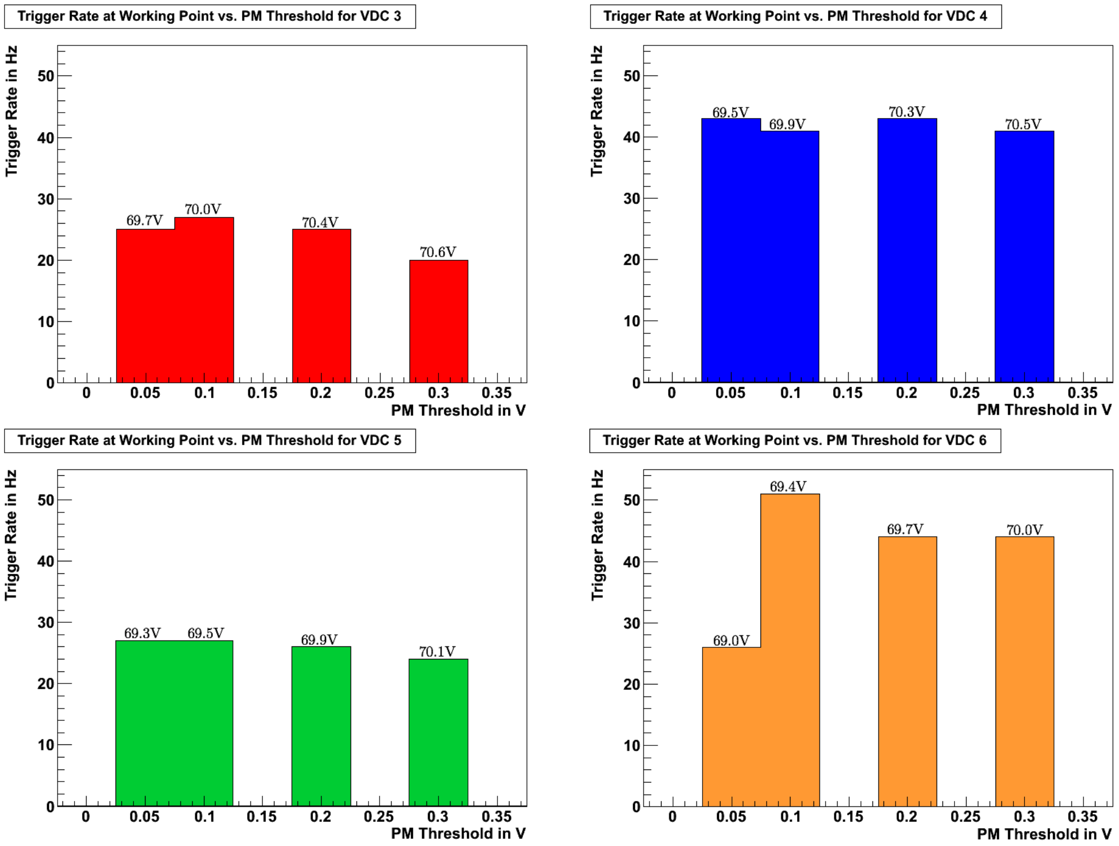

Figure 17: These four plots show the trigger rates versus the PM threshold. A statistical uncertainty of the rates is present due to the fact that only one measurement has been analysed. The SiPM voltages of the different working points are given on top of each column.

It can also be seen in the plot that the trigger rate is about eleven times smaller than the expected trigger rate of $2{\cdot}169\,\mathrm{Hz} = 338\,\mathrm{Hz}$ (sec. 3.2.1 on page 14). Probably less than a third of the electrons have enough energy to reach the scintillating fibre and are able to generate an optical pulse (photon). In addition, the trigger rates are constant at different levels from 24 Hz to 44 Hz. These different levels are not related to the height of the SiPM voltage at the working point (compare fig. 17). More likely, this difference is caused by the different characteristics of the VDCs although they have been built in the same way. However, the number of events is sufficient for the determination of the drift velocity.

Unfortunately, the working point could only be determined for four out of six trigger boxes. No VDC was installed on position one and the trigger rate of VDC 2 seems to be identical to the anode rate due to a wrong response of the adjacent channels inside the NIM-to-ECL converter which is responsible for forwarding the signals to the TDC[17]. All other signal paths at the outside have been controlled several times. Therefore, no working point could be determined, because the anode rate is greater than the trigger rate in the region that is analysed to determine the working point.

3.4 Test of Stability over Time

This kind of measurement shows the development of different counting rates over time so that a statement can be made about the stability of the results during continuous operation. Furthermore, it can be observed whether there is an impact on the measurements from the outside, like the temperature, or not.

3.4.1 Run Type HISTORY

To verify the stability of the counting rates, the operating voltages of the anode, cathode and both SiPMs are set at a fixed value for the entire time of the measurement. Then the rates are recorded several times in a preset time interval.

The following plot shows a measurement that has been taken over the weekend with a voltage of 1850 V for the anode, −14 kV for the cathode and “nominal HV “ for both SiPMs (tab. 6 on the preceding page). The counting time interval has been set to 500 s in order to avoid statistical fluctuations in the rates.

---

[17] Time to Digital Converter

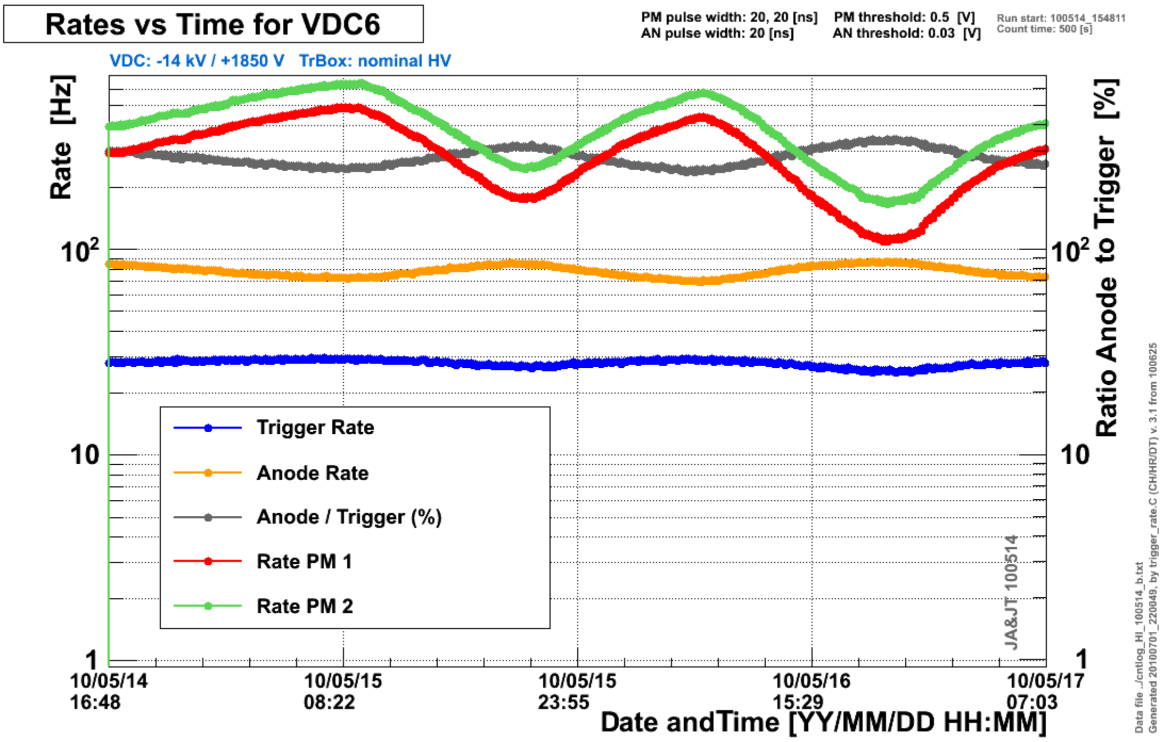

Figure 18: The development of different rates over time is observed in this plot. The cathode voltage is set to −14 kV and the anode voltage to 1850 V.

3.4.2 Results of Counting Rates vs. Time

Looking at figure 18, it is striking that the counting rates of PM 1 and 2 vary over a half order of magnitude over the entire weekend. This fact has not been noticed during other measurements, because they are too short in time and parameters are changed often (e.g. the SiPM voltage during run type PM). However, the trigger rate is not affected by the variation of the PM rates and is almost constant. This indicates, that the change in the counting rates of the SiPMs is due to noise. Having in mind that the SiPMs are responding sensitively to temperature, it is necessary to compare the counting rates with the temperature profile.

3.4.3 Comparison to Temperature Profile

There are five temperature sensors close to the trigger box. Two are installed inside the trigger box and three around the gas manifold (GM). In order to analyse the data, the software programme “temperature.c” was written with the help of Carsten Heidemann [8]. Plot 19 shows the results.

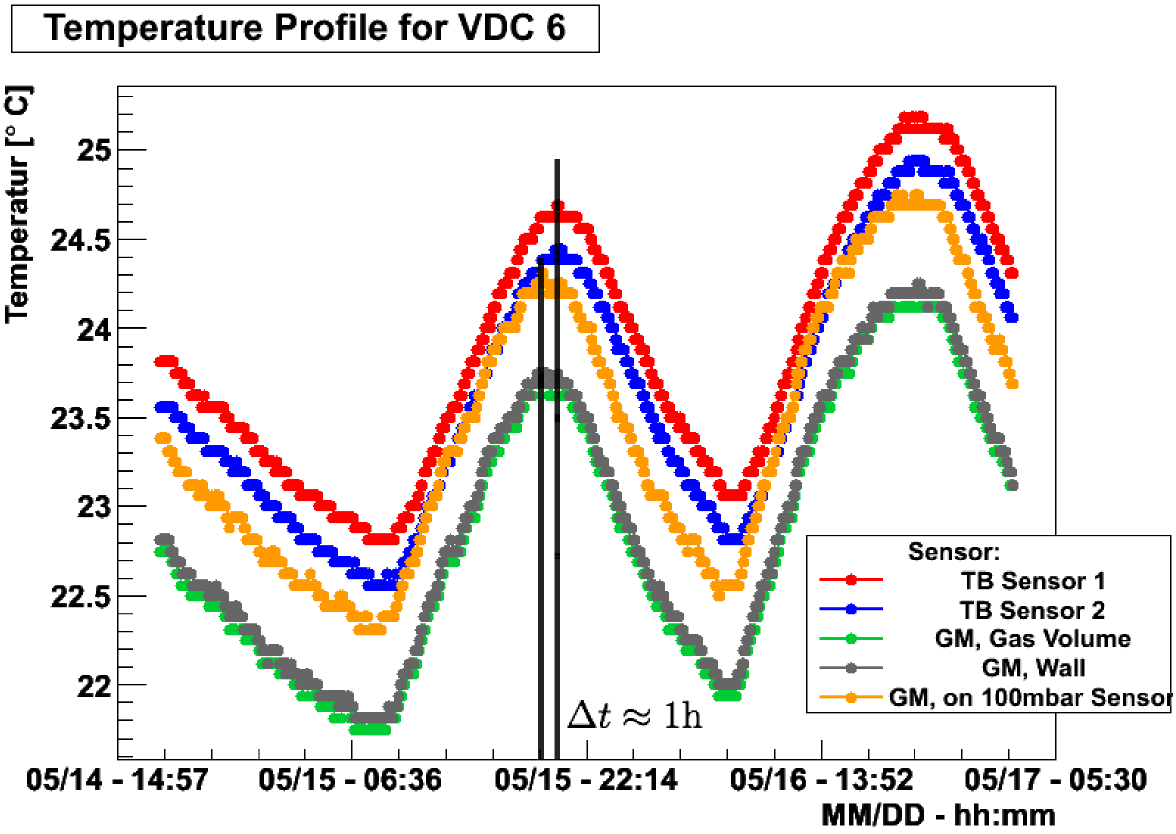

Figure 19: The variation of the temperature over time for different sensors installed on the inside and outside of the trigger unit can be observed in this plot.

Comparing the temperature curves with each other, only a small delay in time between the peaks of the temperature curves can be observed ($\Delta t \approx 1\,\mathrm{h}$). It shows that the temperature at the inside and outside of the VDC/trigger box changes almost at the same time. The small delay is due to the fact that metal conducts warmth faster than air: three sensors are installed on the gas manifold, i.e. on metal, and two inside the trigger box that are surrounded by air.

Though, comparing the temperature profile with the PM rates over time, it can be observed that their development is exactly the opposite. This result contradicts the general expectation that the counting rates are increasing when the temperature is increasing, too.

3.4.4 Results of Comparison

The most important and most positive result is that the trigger rate is constant over time, even when a change in temperature in the environment of the chamber has an impact on the PM counting rates. It is also a proof for the effectiveness of the trigger system to suppress noise.

A suggestion [12] can be made why the counting rates of both SiPMs behave contradictorily regarding the expectation:

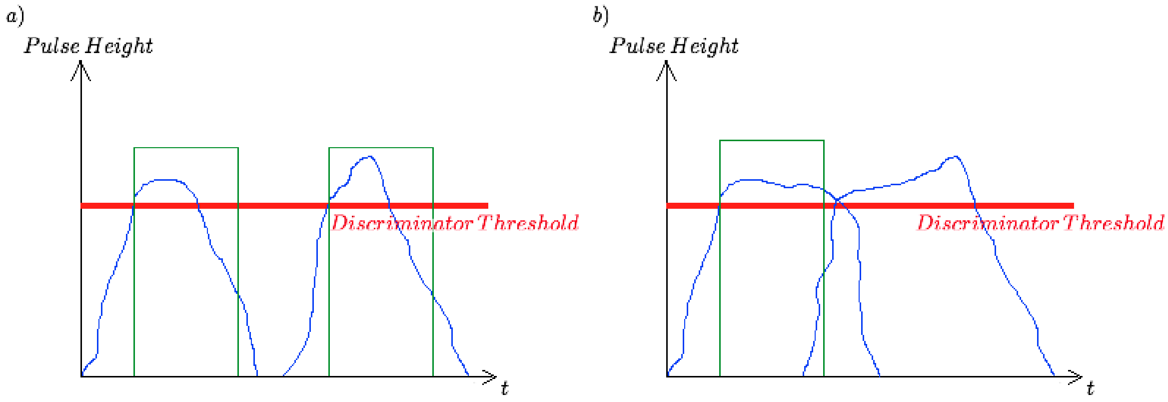

Figure 20: a) shows the expected registration of an incoming pulse at the discriminator that is converted to a NIM-pulse. b) shows two overlapped incoming pulses so that two signals are converted to one NIM-pulse.

Usually, shown in figure 20 a) at the discriminator every pulse from the SiPMs (blue) produces a rectangular signal (green) when the pulse height becomes greater than the discriminator threshold. There every pulse is registered and can be counted separately. However, when the temperature outside increases the pulse widths of the PM signals increase, too. The two incoming, long pulses overlap (fig. 20 b)) so that their amplitudes do not drop below the discriminator threshold and they are only registered as one pulse. This leads to a decreasing counting rate, because two pulses are more often registered as one. To verify this hypothesis, the shape of the pulses has to be analysed, but such a device has not been available.

3.5 Test Pulse Unit

In the future when the VDC system is at CERN, a test pulse unit is going to be operated via computer and is going to be used for telediagnoses, because an expert on the VDC system cannot always be expected to be on duty. The test pulse unit that is used in the following measurements is a prototype (fig. 21) which is able to vary the shape of a rectangular pulse in height and width. For the analysis and determination of errors it is possible to use four inlets on the VDC into which these test pulses can be fed: the LED mounted on the trigger box, the connecting block of the anode and the preamplifiers of both SiPMs [8]. Another possible utilization for the prototype is to test the efficiency of the trigger system and to analyse the influence of the test pulse amplitude on the SiPM counting rates while the SiPM supply voltage is varied.

3.5.1 Experimental Set-Up and Functioning

A timing unit generates the frequency of the test pulses. This signal is fed into the test pulse unit (In) and is used as a start signal for a pulse of which the amplitude and the pulse width can be adjusted with spindle potentiometers. With a switch the user can choose between two settings (A and B) which, for example, allow a fast change between two preset pulse heights. There are multiple outlets (8 x Out) in order to test the six VDCs and other parts simultaneously.

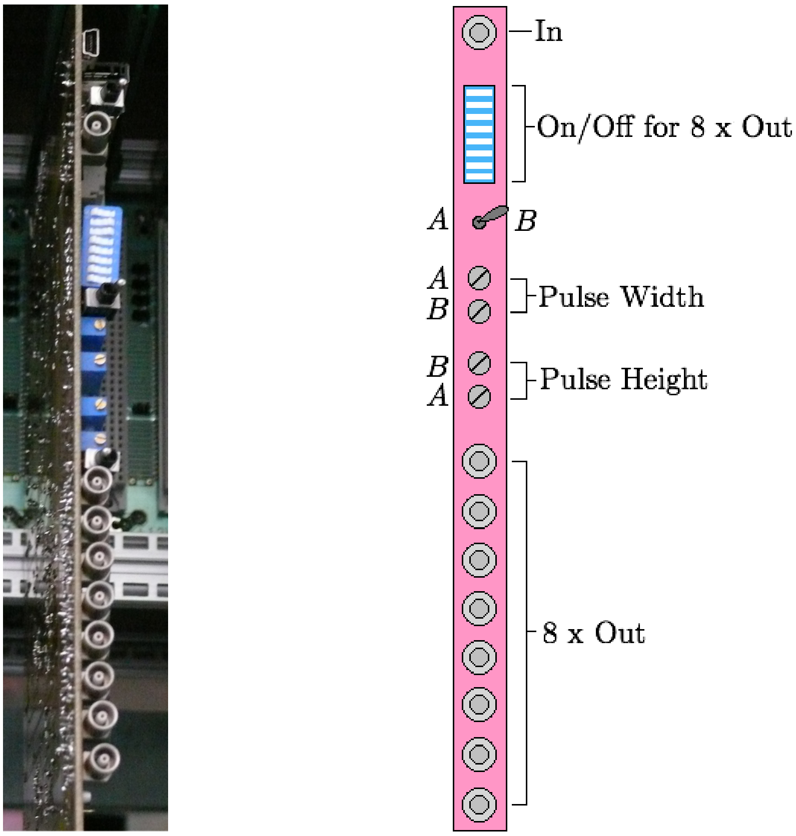

Figure 21: The photograph on the right shows the test pulse unit prototype that is used in all following measurements. The sketch on the left shows the front of the test pulse unit and roughly explains its components.

This unit can also be used to test the effectiveness of the SiPMs as well as the coincidence module and to observe their behaviour while counting. Therefore the test pulses are fed into the LED that is mounted on the trigger box in order to create optical pulses. The radioactive sources can stay inside the chamber, because the amount of light pulses created by the β^--decay electrons is small compared to the adjusted test pulse rate and can therefore be neglected.

3.5.2 Variation of Pulse Width

In all measurements a frequency of 100 kHz for the test pulses is set. With this quantity, the maximum pulse width can be calculated:

$$\begin{aligned} 100\ \text{kHz} &\Rightarrow 100\,000\ \text{pulses per s} \\ &\Rightarrow 10^{-5}\ \text{s per pulse} \qquad (16) \end{aligned}$$

It should not be greater than 10 µs in order to register all incoming optical pulses. When the pulse width is greater than 10 µs not every incoming pulse can be observed and the counting rates are decreasing. A plot with this effect cannot be shown because the test pulse unit is not able to widen the pulses enough or to deal with higher frequencies than 100 kHz. However, it is the same effect that is described in figure 20b).

In all following measurements the pulse width is set to 25 ns to have more than enough scope to register all incoming optical pulses.

3.5.3 Variation of Pulse Amplitude

The transition from small to large pulse amplitudes is examined on the basis of VDC 2 (all other chambers behave similarly) while the SiPM voltage varies from 68.1 V to 71.4 V. In figure 22, the height of the LED test pulse (2.2 V) is too small to be registered by the SiPMs. Only a typical behaviour (fig. 13 on page 19) of the source and the noise of the trigger box can be seen.

Some of the optical pulses are registered when the amplitude is set to 2.3 V (fig. 23). Both counting rates and the trigger rate have increased for lower SiPM voltages (≤70 V). A proof that the LED pulses have caused this increase is due to a higher trigger rate: All optical pulses have to travel the same distance through the scintillating fibre and therefore they arrive simultaneously at the SiPMs. This fact is the prerequisite of the coincidence module to generate a trigger count. For higher SiPM voltages the noise of the trigger box is dominant.

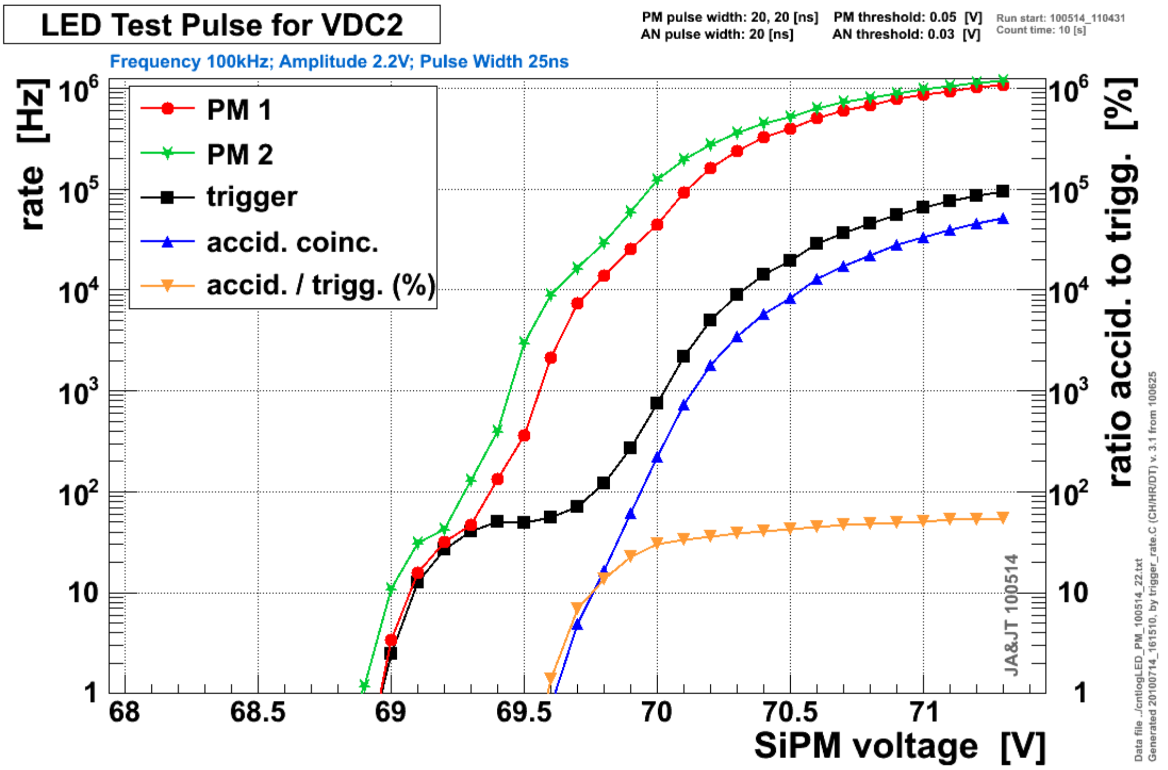

Figure 22: The LED test pulse amplitude is set to 2.2 V with a frequency of 100 kHz and a pulse width of 25 ns. The count time for each measurement point is set to 10 s.

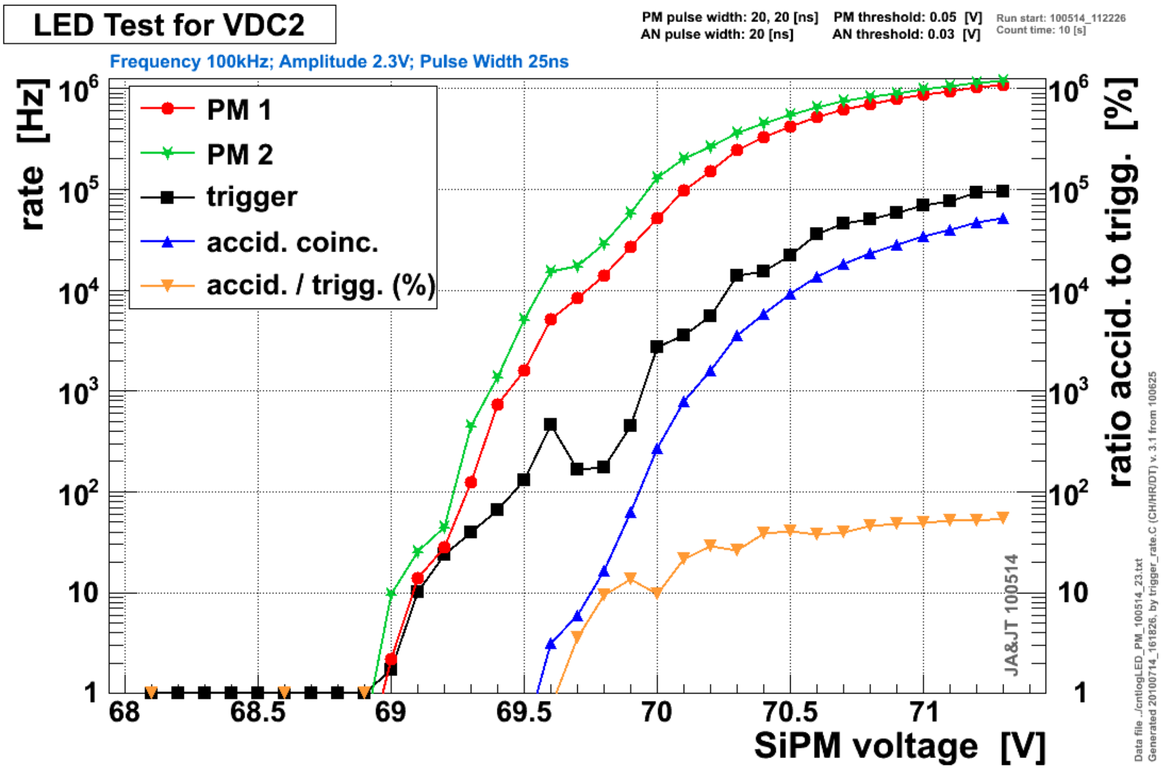

Figure 23: The LED test pulse amplitude is set to 2.3 V with a frequency of 100 kHz and a pulse width of 25 ns. The count time for each measurement point is set to 10 s.

At a pulse height of 2.4 V and a SiPM voltage of 68.9 V (fig. 24) a rapid rise of the counting rates can be observed. From there, the rates fluctuate around the test pulse frequency of 100 kHz. For higher SiPM voltages (≥70 V) the trigger rate almost remains the same, whereas the SiPM rates are dominated by noise.

In the following plot (fig. 25) the same behaviour pattern can be observed for a pulse height of 2.5 V. However for small SiPM voltages the counting rates are constant at the test pulse frequency. Looking closer at the edges in figures 24 and 25, a small shift towards lower SiPM voltages can be seen. This indicates that a lower SiPM voltage is sufficient to register optical pulses with higher amplitudes. Plot 26, in which the amplitude is set to a maximum of 4.8 V, supports this thesis because the edge of the graph is out of the measurement range.

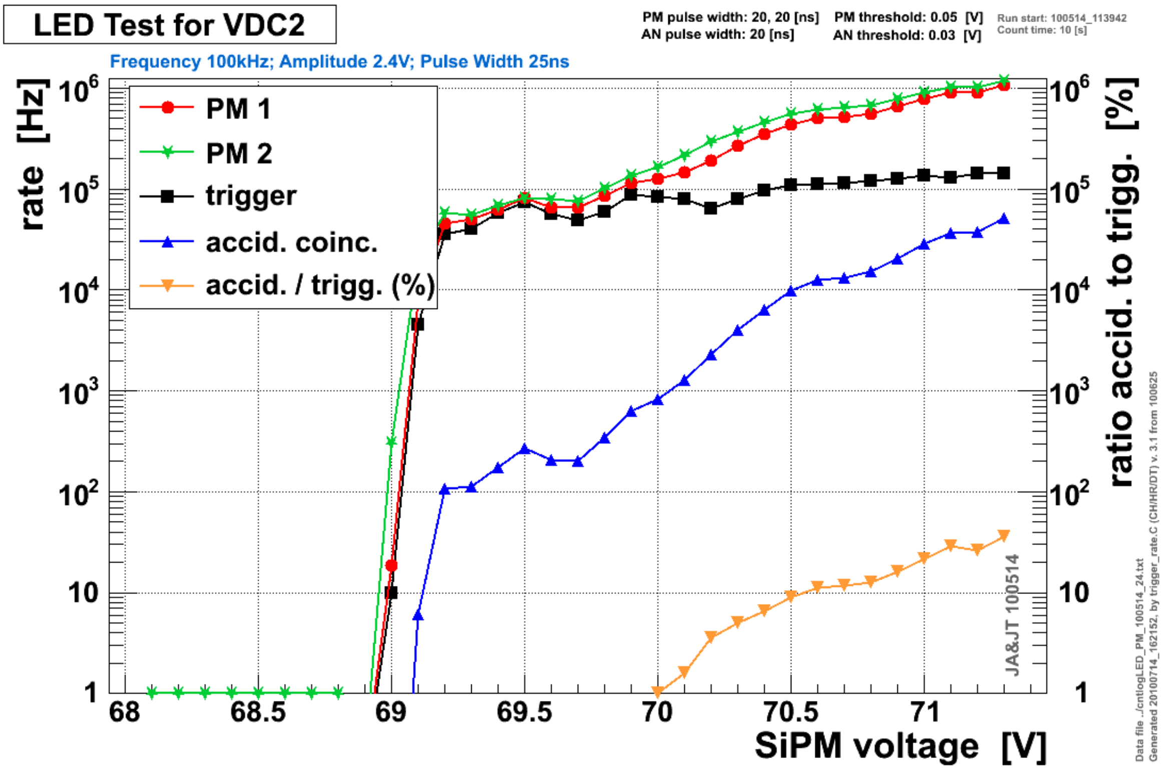

Figure 24: The LED test pulse amplitude is set to 2.4 V with a frequency of 100 kHz and a pulse width of 25 ns. The count time for each measurement point is set to 10 s.

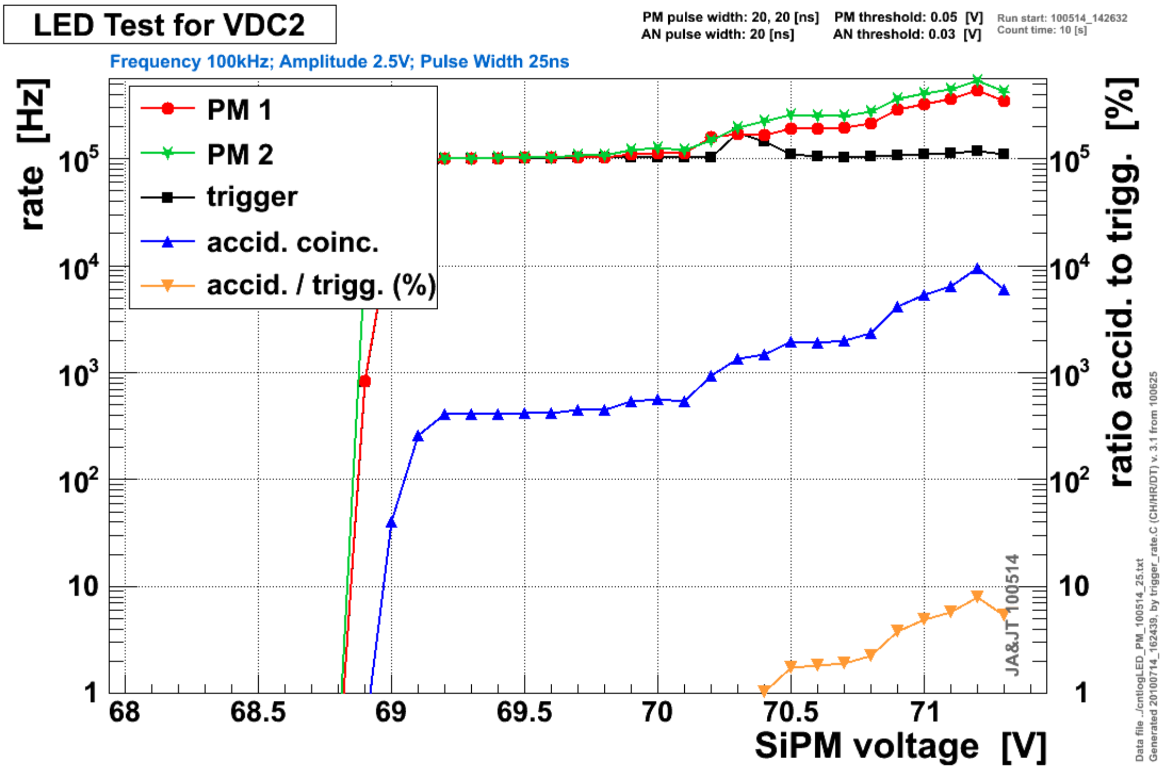

Figure 25: The LED test pulse amplitude is set to 2.5 V with a frequency of 100 kHz and a pulse width of 25 ns. The count time for each measurement point is set to 10 s.

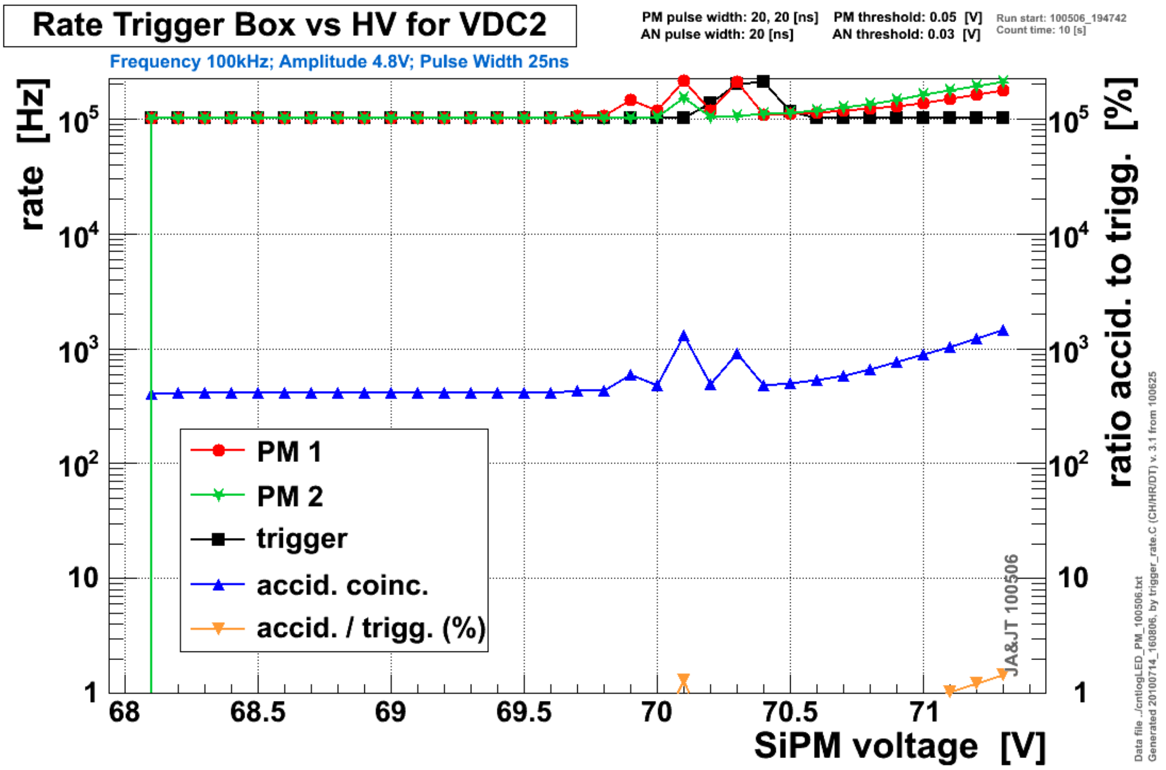

Figure 26: The LED test pulse amplitude is set to 4.8 V with a frequency of 100 kHz and a pulse width of 25 ns. The count time for each measurement point is set to 10 s.

At this pulse height, all VDCs have a constant trigger rate for the range of the SiPM voltage. Also the PM rates are constant (at the same rate than the trigger), up to the point (about 70.5 V) where the noise rate becomes greater than the preset test pulse frequency. Only VDC 2 shows unusual peaks which have been reproduced several times. They have to originate from the radioactive sources, because they disappeared when all test pulse measurements are repeated without the Sr^{90} sources inside the VDCs (fig.27). All other measurements without radioactive sources are almost the same like the ones shown below, so there is no further need to discuss them here.

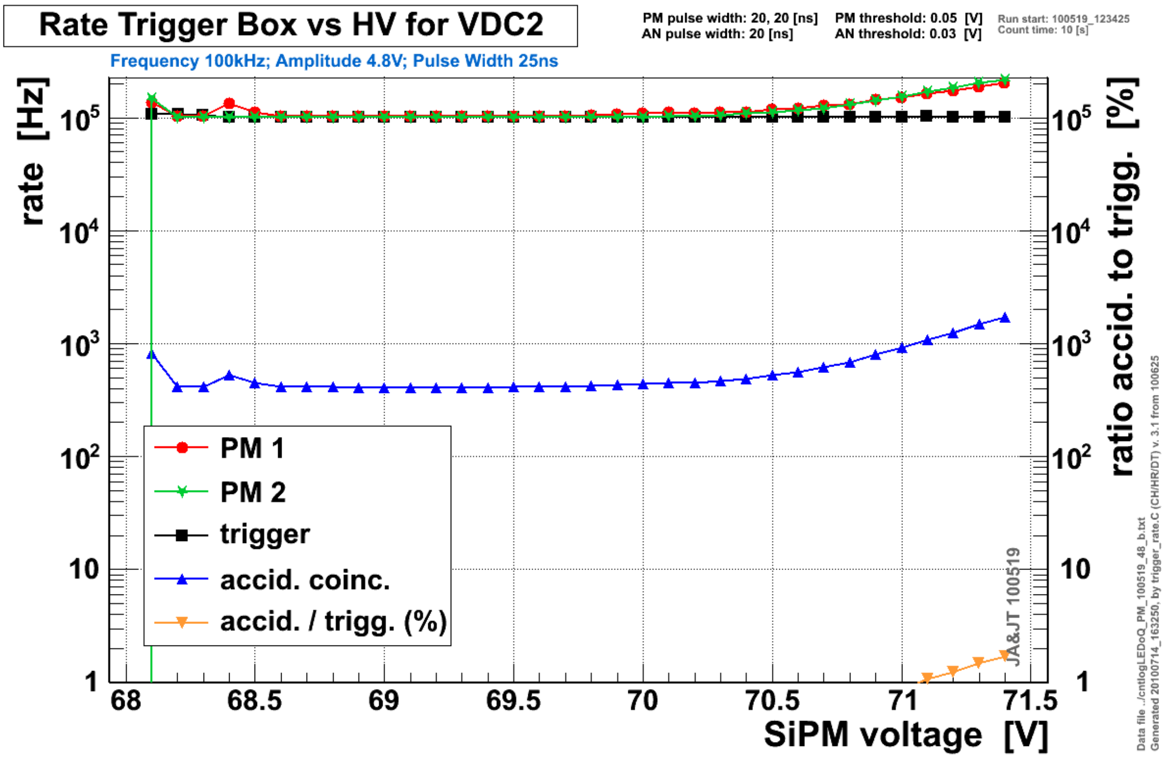

Figure 27: This is a noise measurement with LED test pulses for VDC 2 in which the Sr^{90} sources are not installed inside the VDC. The pulse amplitude is set to 4.8 V. The count time for each measurement point is set to 10 s.

A possible explanation for these extra peaks is the fact that some pulses are counted twice, i.e. the opposite phenomenon to the observation in section 3.4.4 on page 26.

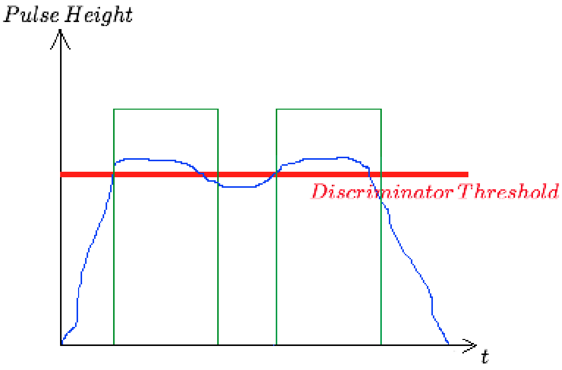

Figure 28: This sketch shows the possible instance that one long pulse is registered as two.

A pulse from the SiPMs (blue) can be longer than the generated NIM-pulse (green) at the discriminator, because this signal is proportional to the amount of detected photons that in this case originate from the test LED. Furthermore the amplitude varies in height due to after pulses so that it can drop below and rise again above the discriminator threshold (fig. 28). Then a second NIM-pulse is generated from the same signal. A proof for this hypothesis is that the trigger and PM rates at these extra peaks are about twice as high as usual (fig. 26).

3.5.4 Results

The efficiency P_E (in %) of the coincidence module can be calculated with the rates that are counted for each measurement. The frequency that has been generated with the timing unit also has been fed into a surplus channel and therefore recorded in order to obtain the actual preset rate.

$$P_E = \frac{\text{trigger rate}}{\text{frequency}} \cdot 100\% \tag{17}$$

The data are taken at a SiPM voltage of 69.5 V and a LED pulse amplitude of 4.8 V. VDC 1 has not been installed at the time of the measurement.

VDC #	1	2	3	4	5	6
P_E in %	n/a	99.9839	99.9797	99.9791	99.9999	99.9958

Table 7: The efficiency P_E of trigger system for LED test pulses with an amplitude of 4.8 V and a duration of 25 ns at frequency of 100 kHz is listed in this table. The Sr^{90} sources were present during the measurement.

As it can be seen in the table, all SiPMs detect the optical pulses from the LED very effectively.

4 Conclusions and Outlook

The influence of the temperature on the SiPMs and the resulting change in their counting rates is shown. However, it has been observed that this variation does not affect the trigger rate, so that a stable and steady rate is obtained by using a coincidence module. Also, the efficiency of both SiPMs to see almost all incoming optical test pulses is proven. Furthermore, the capability of differentiation between real signals and noise has been estimated and can be assessed as being efficient. In addition, a linear coherence between the SiPM voltage and the noise and trigger rate has been observed. The working point of the SiPMs increases exponentially with the height of the PM threshold. Therefore it is not sufficient to choose one working point for all settings. But the resulting trigger rate is nearly constant for the different PM thresholds.

An improvement for the results that are described above would be to repeat all measurements regarding the determination of the working point several times so that mean values and statistical errors can be calculated.

With the results of Jennifer Arps' and this bachelor thesis all parameters that affect the drift time measurement, i.e. the rates of the anode and the trigger, are set. Now, the analysis of the drift velocity in gases with different impurities can be started. Also, there is a need for further computer programmes that are able to control the parameters of the measurement system and to analyse, for example, the drift time data during the time of continuous operation of the VDCs at CERN.

References

[1] Jennifer Arps, Measurements of the drift velocity in drift velocity chambers (VDC). August 2010, Bachelor Thesis, III. Physikalisches Institut A, RWTH Aachen.

[2] George Altenhöfer, Development of a Drift Chamber for Drift Velocity Monitoring in the CMS Barrel Muon System. May 2006, Diploma Thesis, III. Physikalisches Institut A, RWTH Aachen.

[3] A. Böhm et al., Drift Velocity Monitoring for the L3 Experiment, Aachen 1989.

[4] Wolfgang Demtröder, Experimentalphysik Band 4: Kern-, Teilchen- und Astrophysik. Sringer Verlag, 2008.

[5] Hamamatsu, `http://jp.hamamatsu.com/resources/products/ssd/pdf/s10362-11series_kapd1022e05.pdf` (retrieved on 07/11/2010)

[6] Thomas Hebbeker, Elementarteilchenphysik (Lecture SS 2010), III. Physikalisches Institut A, RWTH Aachen.

[7] Thomas Hebbeker, Vorbereitungskurs zum Physikalischen Fortgeschrittenenpraktikum: Statistik Teil I (Lecture WS 2009/2010), III. Physikalisches Institut A, RWTH Aachen.

[8] Carsten Heidemann, Beiträge zur direkten Messung der Driftgeschwindigkeit im Gas der Myonenkammern am CMS-Experiment. July 2010, Diploma Thesis, III. Physikalisches Institut A, RWTH Aachen.

[9] Jens Frangenheim, Measurements of the drift velocity using a small gas chamber for monitoring of the CMS muon system. June 2007, Diploma Thesis, III. Physikalisches Institut A, RWTH Aachen.

[10] C. Amsler et al. (Particle Data Group), The Review of Particle Physics, Physics Letters B667, 1 (2008) and 2009 partial update for the 2010 edition.

[11] Oliver Pooth, Vorbereitungskurs zum Physikalischen Fortgeschrittenenpraktikum: Strahlenschutz (Lecture WS 2009/2010), III. Physikalisches Institut A, RWTH Aachen.

[12] Hans Reithler, 2010, private communications, III. Physikalisches Institut A, RWTH Aachen.

[13] `http://www.kosmologs.de/kosmo/gallery/6/CERN_all-experiments.jpg` (retrieved on 31/07/2010)

[14] `http://web.physik.rwth-aachen.de/~fspcms/FSP-CMS/images/original/cms_detector_3d_english.jpg` (retrieved on 31/07/2010)

[15] `http://cms.web.cern.ch/cms/Detector/Tracker/Pixels.html` (retrieved on 31/07/2010)

[16] `http://cms.web.cern.ch/cms/Detector/Muons/index.html` (retrieved on 31/07/2010)

[17] `http://www.lhc-facts.ch/index.php?page=cms` (retrieved on 31/07/2010)

List of Tables

List of Figures